Genetically defined nucleus incertus neurons differ in connectivity and function

Emma D. Spikol,[1, 2] Ji Cheng,[2] Michelle Macurak,[3] Abhignya Subedi,[3] and *Marnie E. Halpern[1, 2]

*Corresponding author: Marnie.E.Halpern@dartmouth.edu

[1] Department of Neuroscience, Johns Hopkins University School of Medicine, Baltimore, MD 21205, USA

[2] Department of Molecular and Systems Biology, Dartmouth College, Geisel School of Medicine, Hanover, NH 03755, USA

[3] Department of Embryology, Carnegie Institution for Science, Baltimore, MD 21218, USA

SUMMARY

The nucleus incertus (NI), an understudied hindbrain structure implicated in the stress response, arousal, and memory, is a major site for production of the neuropeptide relaxin-3. On the basis of *goosecoid homeobox 2* (*gsc2*) expression, we identified a neuronal cluster that lies adjacent to *relaxin 3a* (*rln3a*) neurons in the zebrafish analogue of the NI. To delineate properties of the *gsc2* and *rln3a* neurons, we used CRISPR/Cas9 targeted integration to drive gene expression in each group, and showed that they differ in afferent input, efferent connections and functional properties. *gsc2* and *rln3a* NI neurons innervate distinct subregions of the interpeduncular nucleus (IPN), but only *gsc2* neurons receive reciprocal innervation from the IPN. Whereas *gsc2* neurons are activated by electric shock, *rln3a* neurons exhibit spontaneous fluctuations in calcium signaling and regulate locomotor activity. Our findings define heterogeneous neurons in the NI and provide new tools to probe its diverse functions.

Keywords: zebrafish, relaxin-3, goosecoid 2, interpeduncular nucleus, locomotion

INTRODUCTION

The nucleus incertus (NI) was originally identified in the human brain (Streeter, 1903) and consists of bilaterally paired clusters of neurons at the midline of the floor of the fourth ventricle (Olucha-Bordonau et al., 2018; Ma and Gundlach, 2015). A variety of neuropeptides have been detected in the region, including cholecystokinin (Kubota et al., 1983; Olucha-Bordonau et al., 2003), neuromedin B (Lu et al., 2020), neurotensin (Jennes et al., 1982), and relaxin-3 (Burazin et al., 2002; Smith et al., 2010), however, the heterogeneity of neuronal subtypes and their functions are poorly understood. In rodents, the NI contains the largest population of neurons in the brain that produce relaxin-3 (RLN3) (Ma et al., 2017; Tanaka et al., 2005; Smith et al., 2010; Smith et al., 2011) a neuropeptide thought to mediate behavioral responses to aversive stimuli (Lawther et al., 2015; Ryan et al., 2013; Zhang et al., 2015). Although some NI neurons do not produce RLN3 (Ma et al., 2013), their characteristics are not well distinguished from the RLN3 population.

Initial investigations in rodents indicate that the NI responds to stressful cues; NI neurons are enriched in receptors for the Corticotropin Releasing Factor (CRF) and upregulate c-Fos in response to CRF exposure (Potter et al., 1994; Bittencourt and Sawchenko, 2000). Placement in an elevated plus maze, exposure to an anxiogenic drug, foot shock, or water-restraint stress also induce c-Fos expression in the NI (Tanaka et al., 2005; Lawther et al., 2015; Passerin et al., 2000; Rajkumar et al., 2016). Moreover, a recent study in mice demonstrates that optogenetic activation of GABAergic neurons in the NI during presentation of an aversive stimulus blocks fear memory formation (Szőnyi et al., 2019). Other reports have implicated the NI in regulating baseline locomotor activity. For example, electrical microstimulation of the NI promotes locomotion in rats (Farooq et al., 2016), and optogenetic activation of a subset of neurons in the mouse NI that produce the neuropeptide neuromedin B increases locomotor speed (Lu et al., 2020). Given the diverse behavioral roles attributed to the NI, we examined neuronal subtypes within it to elucidate their identity and connectivity, and determine whether they mediate specialized functions.

Larval zebrafish are a powerful model to investigate neuronal diversity and connectivity because their transparency and genetic tractability are advantageous for

monitoring and manipulating specific subpopulations. In zebrafish, the presumed analogue of the NI is the griseum centrale, a longitudinally oriented nucleus situated on the ventral surface of the rhombencephalic ventricle, extending partially into the mesencephalon (Olson et al., 2017; Wullimann et al., 1996; Agetsuma et al., 2010). The griseum centrale was suggested to encompass brain regions equivalent to the mammalian NI and periaqueductal grey (PAG) (Olson et al., 2017; Agetsuma et al., 2010). Further work revealed that expression of *relaxin 3a* (*rln3a*) is restricted to two bilaterally paired clusters of neurons in the midbrain and two bilaterally paired nuclei in the hindbrain, bordering the midline (Donizetti et al., 2008). It was proposed that the midbrain *rln3a* expression domains correspond to the PAG, a region that also produces RLN3 in rodents (Ma et al., 2017; Tanaka et al., 2005; Smith et al., 2010), and that the hindbrain *rln3a* neuron clusters correspond to the NI (Donizetti et al., 2008). Zebrafish have a second paralog encoding Relaxin-3, *relaxin 3b* (*rln3b*), which is transcribed by the same PAG neurons that express *rln3a*, but not by neurons in the NI (Donizetti et al., 2009).

The zebrafish griseum centrale is a proposed target of the habenulo-interpeduncular nucleus (Hb-IPN) axis, a highly conserved forebrain to midbrain pathway implicated in modulating anxiety and the response to aversive stimuli (Agetsuma et al., 2010; Facchin et al., 2015; Duboué et al., 2017; McLaughlin et al., 2017). Left-right asymmetry of the habenular region is widespread among vertebrate species (Harris et al., 1996; Ahumada-Galleguillos et al., 2017) and in zebrafish, the left and right dorsal habenulae (LdHb and RdHb) exhibit prominent differences in their molecular properties, connectivity and functions (deCarvalho et al., 2014; Gamse et al., 2005; Facchin et al., 2015; Duboué et al., 2017). The LdHb projects to the dorsal IPN (dIPN) and ventral IPN (vIPN), whereas RdHb neurons largely innervate the vIPN (Gamse et al., 2005). Using tract tracing in adult zebrafish, Agetsuma et al., 2010 found that the dIPN and vIPN also have different targets: the vIPN projects to the dorsal raphe and the dIPN innervates neurons in the hindbrain griseum centrale. However, the precise neuronal populations the LdHb-dIPN pathway targets in the griseum centrale, and specifically in the NI, are unknown.

In this study, we describe a small population of neurons, defined by expression of the *gsc2* gene, that is closely apposed to *rln3a* neurons in the zebrafish hindbrain. Through CRISPR/Cas9-mediated targeted integration, we generated QF2 transgenic driver lines (Riabinina and Potter, 2016; Subedi et al., 2014) to facilitate selective labeling and manipulation of the *rln3a* and *gsc2* neuronal populations. Neurochemical characteristics and connectivity are consistent with NI identity. However, despite their close anatomical proximity in the NI, *gsc2* and *rln3a* neurons differ in their efferent and afferent connectivity, spontaneous activity, responses to aversive stimuli, and control of locomotor behavior. The results demonstrate the power of genome editing to generate precise tools for interrogating the roles of neighboring neurons in understudied regions of the vertebrate brain.

RESULTS

Identification of *gsc2* neurons in the nucleus incertus

The *goosecoid homeobox 2* (*gsc2*) gene encodes a protein which has homology to goosecoid-related proteins in its homeobox domain-containing sequence. We initially identified *gsc2* through transcriptional profiling aimed at distinguishing genes with enriched expression in the midbrain interpeduncular nucleus (IPN). IPN tissue was micro-dissected from the brains of adult zebrafish harboring *TgBAC(gng8:Eco.NfsB-2A-CAAX-GFP)*^{c375}, a transgene that labels dorsal habenular neurons and their axons with membrane-targeted GFP in larvae and adults. Because GFP-labeled dHb axon terminals demarcate the IPN, they serve as a guide to locate and excise this midbrain structure (deCarvalho et al., 2013). After comparing the transcriptional profile of pooled IPN samples with remaining brain tissue, *gsc2* transcripts were identified as enriched approximately 5-fold in the IPN relative to the rest of the brain. We note that the *gsc2* gene is not annotated in the latest genome assembly (GRCz11) and was identified by aligning reads to Zv9 (Ensembl release 77).

A cluster of neurons in the mouse brain was previously found to express the *Goosecoid-2* gene. However, some reports indicate that neurons expressing *Gsc2* are found within the IPN (Funato et al., 2010; Gong et al., 2003), whereas others suggest that they lie within the pons region (Saint-Jore et al., 1998; Gottlieb et al., 1998). We

examined *gsc2* expression in zebrafish larvae using whole-mount *in situ* hybridization (WISH) and detected transcripts in a cluster of neurons that appear just posterior to the midbrain-hindbrain boundary, and in a few sparsely distributed neurons anterior to this main cluster (Fig. 1A, A'). Double labeling for both *gsc2* and *somatostatin 1.1* (*sst1.1*), the latter being expressed in the IPN (Doll et al., 2011), indicates that in the larval brain, *gsc2* neurons are located dorsal to the IPN, and not within it (Fig. 1B, B').

Owing to the similar positions of *gsc2* and *rln3a* (Donizetti et al., 2008) neurons in the larval hindbrain, we performed double-label WISH, and found that *gsc2* neurons are a distinct population, located anterior to the *rln3a* neurons (Fig. 1C, C', D).

Neuropeptides other than RLN3 have also been detected in the rodent NI, including neuromedin B in mice (Lu et al., 2020), and cholecystokinin (Kubota et al., 1983; Olucha-Bordonau et al., 2003) and neurotensin (Jennes et al., 1982) in rats. To determine whether transcripts encoding each of these neuropeptides are expressed in the zebrafish NI, we performed WISH for the homologous genes *cholecystokinin a* (*ccka*), *cholecystokinin b* (*cckb*), *neuromedin a* (*nmba*), *neuromedin b* (*nmbb*), and *neurotensin* (*nts*) (Supp. Fig. 1A-E'). For cholecystokinin and neuromedin, the combined expression of the two zebrafish paralogues closely resembles the overall expression pattern of each single rodent gene (Albus, 1988; Ohki-Hamazaki, 2000). Only *cckb* and *nmbb* transcripts were detected in the NI, and *nmbb* expression was also observed in the PAG (Supp. Fig. 1B, D). Using double-label fluorescent WISH, we found that *gsc2* neurons did not co-express any of these neuropeptides (data not shown). In contrast, the hindbrain *nmbb* neurons are intermingled with *rln3a* neurons in the NI, with a small subset of neurons expressing both neuropeptides (Fig. 1E, Supp. Fig. 2A'-C''). However, *rln3a* and *nmbb* neurons exist as separate, adjacent populations in the PAG (Supp. Fig. 2A). We also found that hindbrain *cckb* neurons are located just posterior to *rln3a* and *nmbb* neurons (Fig. 1F). The results reveal a map of peptidergic neurons in the zebrafish NI, with a discrete group of *gsc2*-expressing neurons, partially overlapping expression of *rln3a* and *nmbb* in cells posterior to *gsc2* neurons, and a distinct population of *cckb* neurons posterior to the *rln3a* and *nmbb* neurons (Fig. 1G).

gsc2 and _rln3a_ transgenic lines drive expression in the NI

To further verify that the *gsc2* and *rln3a* neurons reside in the zebrafish analog of the mammalian NI, we examined the properties of these closely apposed neuronal populations. Using CRISPR/Cas9-mediated genome integration, we generated transgenic lines to selectively label and manipulate each group. The *gsc2* and *rln3a* loci were independently targeted for integration of sequences encoding *QF2* (Fig. 2A, D), a modified transcription factor that binds to the upstream activating sequence (QUAS) in the bipartite Q transcriptional regulatory system of *Neurospora crassa* (Riabinina and Potter, 2016; Subedi et al., 2014). *Tg(gsc2:QF2)^{c721}* was generated by introducing the *QF2* sequence into exon 2 of the *gsc2* gene through non-homologous end joining (Kimura et al., 2014). A more recently described method for homology-directed integration called GeneWeld (Wierson et al., 2020) was adapted to include a secondary reporter that, together with the *QF2* sequence, was integrated into exon 1 of the *rln3a* gene to produce *Tg(rln3a:QF2; he1.1:YFP)^{c836}*. Identification of *rln3a:QF2* transgenic carriers was facilitated by the *he1.1:YFP* reporter consisting of a promoter from the *hatching enzyme 1, tandem duplicate 1* (*he1.1*) gene driving expression of yellow fluorescent protein in the hatching gland starting at 1 day post-fertilization (dpf). Because *he1.1* labeling is transient, this secondary reporter does not interfere with brain imaging experiments on older larvae (Xie et al., 2012).

Labeling patterns from *Tg(gsc2:QF2)^{721}* and *Tg(rln3a:QF2; he1.1:YFP)^{c836}* driver lines recapitulate endogenous expression patterns of *gsc2* and *rln3a*, respectively, at both larval (Fig. 2B, C, E, F) and adult (Supp. Fig. 3A-G) stages. Consistent with their location in the NI, the *rln3a* neurons are located on the floor of the 4th ventricle (Supp. Fig. 3G). Similarly, *gsc2* neurons are present at the floor of the 4th ventricle, just anterior to the *rln3a* neurons, but are also distributed more ventrally up to the dorsal surface of the raphe nucleus (Supp. Fig. 3C).

Neurotransmitter identity of _gsc2_ and _rln3a_ neurons

In mice (Szőnyi et al., 2019) and in rats (Olucha-Bordonau et al., 2003), the NI contains a large population of GABAergic neurons and *rln3a* neurons are largely GABAergic (Ma et al., 2007; Nasirova et al., 2020). To determine the neurotransmitter identity of the

zebrafish *rln3a* and *gsc2* neurons, we mated doubly transgenic fish bearing *Tg(gsc2:QF2)*^{c721} or *Tg(rln3a:QF2; he1.1:YFP)*^{c836} and a QUAS reporter to transgenic lines that label glutamatergic neurons expressing the *solute carrier family 17 member 6b* (*slc17a6b*) gene (Miyasaka et al., 2009) or GABAergic neurons expressing *glutamate decarboxylase 1b* (*gad1b*) (Satou et al., 2013). We did not observe co-expression of *gsc2* (Fig. 3A) or *rln3a* (Fig. 3C) with the glutamatergic reporter in the NI. In contrast, an average of 82.43 ± 3.52% of neurons co-expressed GFP and mApple-CAAX in *Tg(gad1b:GFP)*^{nn25Tg}; *Tg(gsc2:QF2)*^{c721}; *Tg(QUAS:mApple-CAAX; he1.1:mCherry)*^{c636} larvae (Fig. 3D, D', G). Similarly, in *Tg(gad1b:GFP)nn25Tg*; *Tg(rln3a:QF2; he1.1:YFP)*^{c836}; *Tg(QUAS:mApple; he1.1:CFP)*^{c788} larvae, an average of 80.57 ± 5.57% of neurons co-expressed GFP and mApple (Fig. 3F, F', F'', G). These results indicate that *gsc2* and *rln3a* neurons are predominantly GABAergic, consistent with their NI identity.

To our knowledge, it has not been verified whether *rln3a* neurons in the periaqueductal grey are also GABAergic. We found that *rln3a* neurons in the PAG were not labeled by the glutamatergic reporter (Fig. 3B), whereas an average of 81.67% ± 3.81% showed labeling from the *gad1b* transgene (Fig. 3E, E', E'', G). This suggests that *rln3a* neurons possess similar neurotransmitter identity across neuroanatomical locations.

Distinct projection patterns of *gsc2* and *rln3a* neurons

To compare the projection patterns of *gsc2* and *rln3a* NI neurons, we expressed membrane-tagged fluorescent reporters in each group and acquired optical sections of their labeled efferents using confocal microscopy. At 6 dpf, projections from *gsc2* neurons were prominent in the cerebellum, IPN, raphe, diencephalon, and rostral and caudal hypothalamus (Fig. 4A-E, Supp. Vid. 1). Sparse *gsc2* projections were also found in the medulla (Supp. Vid. 1) and telencephalon (Fig. 4D). Projections from *rln3a* neurons were found in the medulla, IPN, diencephalon, lateral hypothalamus, and optic tectum (Fig. 4F-J), with some axons appearing to pass through the posterior commissure (Fig. 4G, Supp. Vid. 2). Sparse fibers were also observed in the raphe and telencephalon (Fig. 4H, J, Supp. Vid. 2).

Innervation of the IPN by *rln3a* neurons originates solely from the NI cluster, whereas the bulk of axonal projections throughout the brain emanate from *rln3a* neurons in the PAG (Supp. Vid. 2). This was confirmed by two-photon laser ablation of *rln3a* PAG neurons, which greatly reduced fibers in the medulla, diencephalon, hypothalamus and optic tectum, but spared innervation of the IPN (Fig. 4K-L). Reduction of *rln3a* PAG neuronal projections enabled visualization of *rln3a* NI efferents, which exclusively target the IPN (Fig. 4L, Supp. Vid. 3). Accordingly, ablation of *rln3a* neurons solely in the NI eliminated innervation of the IPN without affecting the rest of the *rln3a* neuron projection pattern (Fig. 4K, M). Efferents from *gsc2* neurons were far more extensive than those of *rln3a* NI neurons, and were observed in regions not innervated by any *rln3a* neurons (e.g., cerebellum and caudal hypothalamus). Thus, the closely apposed *gsc2* and *rln3a* NI neurons exhibit widely divergent projection patterns.

To examine *gsc2* and *rln3a* efferent innervation of the IPN more precisely, we used *TgBAC(gng8:Eco.NfsB-2A-CAAX-GFP)*^{c375} or *TgBAC*(*gng8:GAL4FF*)^{c426}*; Tg(UAS-E1B:NTR-mCherry)*^{c264} to delineate the IPN by labeled dHb axon terminals (deCarvalho et al., 2013; Hong et al., 2013; Davison et al., 2007). We confirmed the location of *gsc2* and *rln3a* neuronal cell bodies dorsal to the IPN as visualized by nuclear-tagged reporters (Fig. 5A, A', C', C'). Using membrane-tagged reporters, we identified axonal projections from both populations to the IPN (Fig. 5B, D, E-J). Intriguingly, the NI neurons innervate disparate regions of the IPN: axons of *gsc2* neurons terminate at the vIPN mainly along the midline neuropil (Fig. 5B, E-F', I, K) and axons of *rln3a* neurons terminate at the dIPN (Fig. 5D, G-H', J, K).

Afferent input to the NI from the dHb-IPN pathway

In mice (Lu et al., 2020) and in rats (Goto et al., 2001; Olucha-Bordonau et al., 2003), the NI has reciprocal connections with the IPN. Additionally, Agetsuma et al., 2010 showed that DiI application to the dIPN resulted in labeled fibers in the griseum centrale, which is thought to be analogous to the mammalian NI. Application of DiI to the dIPN of the adult brain labeled fibers in the ventral portion of the griseum centrale, where *gsc2* neurons are located (Supp. Fig. 4A-C'). However, we did not observe any projections to the dorsal portion of the griseum centrale, just below the 4th ventricle,

where *rln3a* neurons are located (Supp. Fig. 3G). These results indicate that *gsc2* neurons receive input from the dHb-IPN pathway, whereas *rln3a* neurons do not.

To confirm this finding, we optogenetically activated the red-shifted opsin ReaChR (Lin et al., 2013; Wee et al., 2019) in dHb neurons using 561 nm light, while recording calcium transients in either *gsc2* or *rln3a* neurons using 488 nm light (Fig. 6A). We used *Tg(UAS:ReaChR-RFP)*^{if50} to express ReaChR under control of *TgBAC*(*gng8:GAL4FF*)^{c426} , which labels dHb neurons that project to the IPN (Hong et al., 2013). To verify successful activation of dHb neurons by ReaChR, we also included *Tg(UAS:GCaMP7a)*^{zf415} to express the calcium indicator GCaMP7a (Muto et al., 2013) in dHb neurons (Fig. 6B, C). Simultaneously, we used *Tg(QUAS:GCaMP7a)*^{c594} to express GCaMP7a in either *gsc2* or *rln3a* neurons under control of *Tg(gsc2:QF2)*^{c721} or *Tg(rln3a:QF2; he1.1:YFP)*^{c836} (Fig. 6B', C').

We first validated activation of dHb neurons by ReaChR (Fig. 6D-D'', F-F''). Next, we showed that ReaChR activation in the dHb increased calcium transients in *gsc2* neurons, as there was greater activation of *gsc2* neurons in response to 561 nm light in ReaChR-expressing larvae than in ReaChR-negative controls (Fig. 6E-E''). By contrast, similar levels of calcium signaling were detected in the *rln3a* NI neurons of ReaChR-expressing larvae and negative controls in response to 561 nm light (Fig. 6G-G''). There was also no statistically significant difference in the activation of *rln3a* PAG neurons between ReaChR-expressing larvae and ReaChR-negative controls (Fig. 6H-H''). These results confirm that *gsc2* neurons receive input from the dHb-IPN axis and *rln3a* neurons do not, indicating that the latter do not directly mediate functions of the dHb-IPN pathway.

Spontaneous and evoked activity differs between *gsc2* and *rln3a* neurons

In rodents, aversive stimuli such as foot shock, air puff, water-restraint stress, the anxiogenic drug FG-7142, and exposure to an elevated plus maze increase neuronal activity in the NI, yet whether these different stimuli activate similar or distinct neuronal subtypes is unclear (Tanaka et al., 2005; Lawther et al., 2015; Passerin et al., 2000; Rajkumar et al., 2016; Lu et al., 2020; Szőnyi et al., 2019). To determine whether *gsc2* and *rln3a* neurons differ in their response to an aversive stimulus, we expressed

GCaMP7a (Muto et al., 2013) in each subpopulation (Fig. 7B, C) and recorded calcium transients upon delivery of a mild electric shock (25 V, 200 ms duration) to immobilized larvae (Fig. 7A) (Duboué et al., 2017). The *gsc2* neurons showed little spontaneous activity, but exhibited an immediate robust increase in calcium transients in response to shock (Fig. 7D, D', Supp. Vid. 4). By contrast, *rln3a* neurons showed more frequent spontaneous fluctuations in activity throughout the recording period (Fig. 7E-E', F, Supp. Vid. 5) and their response to shock was less robust than that of the *gsc2* neurons (Fig. 7G). The *gsc2* and *rln3a* neurons therefore differ in their spontaneous activity and in their sensitivity to an acute aversive stimulus.

Ablation of *rln3a* but not *gsc2* neurons alters locomotor activity

Previous reports have implicated the NI in regulating locomotor activity and proposed that increased activity in the NI after delivery of an aversive stimulus might underlie the animal's locomotor response (Farooq et al., 2016; Lu et al., 2020). Given that the *gsc2* neurons are responsive to an aversive electric shock whereas *rln3a* neurons exhibit spontaneous fluctuations in activity, we examined the functional roles of each population of neurons in both baseline locomotor behavior and the response to electric shock, which elicits immediate hyperactivity in larval zebrafish (Duboué et al., 2017).

With GFP expression as a guide, we used a two-photon laser to selectively ablate the *gsc2* (Fig. 8A, A') or *rln3a* neurons in the NI (Fig. 8B, B') or *rln3a* neurons in the PAG (Fig. 8C-C'") at 6 dpf. We confirmed ablation by WISH (Supp. Fig. 5A, A', D, D'), and verified that *rln3a* NI neurons were spared in larvae with ablated *gsc2* neurons (Supp. Fig. 5B, B'), and, conversely, that *gsc2* neurons were intact in larvae with ablated *rln3a* NI neurons (Supp. Fig. 5C, C'). At 7 dpf, we measured locomotor activity in freely swimming ablated larvae and unablated siblings for two minutes. After recording baseline locomotion, we delivered a single electric shock (25 V, 200 ms duration) to each larva and measured the locomotor response (Duboué et al., 2017).

Larvae that had *rln3a* NI neurons ablated exhibited increased spontaneous locomotor activity (Supp. Vid. 6), swimming a greater distance than unablated controls, larvae with ablated *gsc2* neurons, or larvae with ablated *rln3a* PAG neurons (Fig. 8D-E). The average bout length in larvae lacking *rln3a* NI neurons was greater than in

unablated larvae, or in larvae with ablated *gsc2* or *rln3a* PAG neurons (Fig. 8F) although the number of swimming bouts was similar in all groups (Fig. 8G). This suggests that ablation of *rln3a* NI neurons promotes prolonged periods of movement, rather than increasing the frequency of movement bouts. All groups exhibited hyperactivity immediately following shock (Fig. 8H-I), and statistically significant differences in the response to shock were not detected (Fig. 8I). These findings suggest that neither the *gsc2* neurons nor the neighboring *rln3a* neurons are required for the immediate behavioral response to shock, whereas *rln3a* neurons in the NI serve to modulate spontaneous locomotor activity.

DISCUSSION

Although first described in the human brain in 1903 (Streeter, 1903), the nucleus incertus ('uncertain nucleus') remains an enigmatic structure that has been implicated in stress (Tanaka et al., 2005; Lawther et al., 2015; Potter et al., 1994; Bittencourt and Sawchenko, 2000; Passerin et al., 2000; Rajkumar et al., 2016), arousal (Lu et al., 2020) and memory (Szőnyi et al., 2019; Ma et al., 2009). As the NI is the primary source of relaxin-3 expressing neurons in the rodent brain, they have been a primary focus of study despite the fact that not all NI neurons produce this neuropeptide (Ma et al., 2013; Nasirova et al., 2020). In this study, we compared the properties of the relaxin-3 expressing cells with an adjacent group of neurons in the NI. Capitalizing on CRISPR/Cas9 technology to generate neuron-specific transgenic lines, coupled with laser-mediated cell ablation, calcium imaging, and optogenetics, we show that the two NI populations have distinct connections with the interpeduncular nucleus and other brain regions, and also differ in their spontaneous activity and influence on behavior. Owing that the NI has been proposed to act together with the median raphe and IPN, in "a midline behavior control network of the brainstem" (Goto et al., 2001), it is important to build the framework of neuronal subtypes that mediate such coordinated activity.

Through transcriptional profiling, we identified *gsc2* as having enriched expression in dissected IPN samples relative to the rest of the adult zebrafish brain. However, upon examining the location of the *gsc2*-expressing neurons, we discovered that they reside outside of the IPN, just anterior to the *rln3a* neuronal cluster. Thus, we

suspect that contamination of IPN samples isolated from the adult zebrafish brain with overlying NI tissue was the source of abundant *gsc2* transcripts. *Gsc2*-expressing neurons have also been identified in the mouse brain, although there is conflicting information about their precise anatomical location (Funato et al., 2010; Gong et al., 2003; Saint-Jore et al., 1998; Gottlieb et al., 1998). On the basis of our results, it is unlikely that they are located within the IPN as had been previously concluded (Funato et al., 2010; Gong et al., 2003).

Previous studies examined the electrophysiological properties (Ma et al., 2013) and connectivity (Nasirova et al., 2020) of RLN3-negative neighbors of RLN3 neurons, but these neurons are intermingled with those that produce Rln3 and likely produce other known NI neuropeptides (Nasirova et al., 2020). For example, in mice, *Rln3* and *Nmb* are expressed in interspersed neuronal populations and are co-expressed in a subset of cells (Lu et al., 2020; Nasirova et al., 2020) in a similar pattern observed for *rln3a* and *nmbb* neurons in the NI of larval zebrafish. By mapping the location of neuropeptide-expressing neurons within the NI, we confirmed that the *gsc2* cluster is distinct from cells producing relaxin-3, neuromedin B, or cholecystokinin.

Functional specialization of NI neurons

Targeted CRISPR/Cas9-mediated genome editing enabled us to generate transgenic lines to label and manipulate *gsc2* and *rln3a* neurons selectively and elucidate their characteristics. We found that their anatomical location, neurotransmitter phenotype, and hodological properties are consistent with NI identity; both groups of neurons are GABAergic, reside on the floor of the fourth ventricle and project to the IPN. However, these adjacent neuronal populations differ in their activity and connectivity (summarized in Table 1). Perturbation of *rln3a* NI neurons increases spontaneous locomotion, whereas disrupting the adjacent *gsc2* neurons does not, suggesting that the distinct properties of the *gsc2* and *rln3a* neurons underlie disparate functions.

Rodent studies have described the behavior of animals with null mutations in the gene encoding RLN3 (Smith et al., 2012), or its receptor, RXFP3 (Hosken et al., 2015), and found decreases in voluntary wheel running, which suggests that the relaxin-3 system is involved in regulating locomotor activity. However, it is difficult to attribute

mutant phenotypes to specific groups of *Rln3* neurons. Farooq et al., 2016 found that microstimulation targeted to the NI induced movement in rats, which implicates the NI region in regulating locomotor activity but does not elucidate the relevant neuronal population. To this point, it was reported that activation of *Nmb* neurons in the mouse NI promotes locomotion, highlighting the importance of direct modulation of specific neuronal subgroups (Lu et al., 2020).

We show that ablation of *rln3a* neurons specifically in the NI results in hyperactivity of zebrafish larvae, whereas ablation of adjacent *gsc2* neurons, or *rln3a* neurons in the PAG, does not affect locomotion. This suggests that the role of the NI in regulating baseline locomotor activity is mediated by *rln3a* neurons. Because some *nmbb* neurons are interspersed with *rln3a* neurons in the NI, we cannot eliminate the possibility that loss of *nmbb* neurons also contributes to the hyperactivity phenotype. Strikingly, whereas previous studies in adult rodents indicate that NI activity promotes locomotion, we find the opposite in larval zebrafish; NI neurons normally suppress spontaneous locomotor activity. Interestingly, a study of dopaminergic signaling in larval zebrafish found that dopamine suppressed spontaneous fictive swim episodes (Thirumalai and Cline, 2008), although dopamine is classically known for stimulating locomotor activity (Ryczko and Dubuc, 2017). Differential roles for neuromodulators during development and adulthood could be a general feature of locomotor circuitry and may be crucial for neural circuit maturation, a possibility that should be further investigated.

We recorded different patterns of activity in neuronal populations of the NI that have not been previously identified: *gsc2* neurons have little spontaneous activity, whereas *rln3a* neurons exhibit continuous fluctuations in calcium signaling. A previous study in rats found that relaxin-3 neurons fire in synchrony with the ascending phase of the hippocampal theta oscillation (4-12 Hz), which has been implicated in spatial memory (Ma et al., 2013). Stimulation of NI neurons in rats and *Nmb* NI neurons in mice has been shown to increase hippocampal theta power (Nuñez et al., 2006; Lu et al., 2020). However, the oscillating calcium transients that we detected in *rln3a* neurons of larval zebrafish are on the order of seconds, consistent with infra-slow waves that occur at frequencies in the range of tens to hundreds of seconds, and within which fast

oscillations are often nested (Palva and Palva, 2012). Infra-slow oscillations correlate with rhythmic fluctuations in human performance observed in psychophysical experiments, in which a subject performs a task of constant difficulty for several minutes. It has been proposed, therefore, that intra-slow waves coordinate shifts between attentive and inattentive brain states (Palva and Palva, 2012). Given that ablation of *rln3a* NI neurons increases the length of movement bouts in zebrafish larvae, fluctuating activity in *rln3a* neurons may control transitions between phases of behavioral activity and inactivity.

Revisiting the NI response to aversive stimuli

A number of studies have found that aversive stimuli promote expression of c-Fos in the NI (Tanaka et al., 2005; Lawther et al., 2015; Passerin et al., 2000; Rajkumar et al., 2016), leading researchers to evaluate the role of relaxin-3 in anxiety-like behavior. In rats, intracerebroventricular infusion of a relaxin-3 receptor agonist increased entries to the open arms of an elevated plus maze and the amount of time animals spend in the light portion of a light-dark box (Ryan et al., 2013). Similar assays in mice showed that the relaxin-3 receptor agonist did not alter the basal behavioral state but rather reduced the anxiety-like behavior induced by the anxiogenic drug FG-7142 (Zhang et al., 2015). However, a role for the NI in regulating the behavioral response to acute aversive stimuli has so far not been described. Lu et al., 2020 note that *Nmb* neurons in the mouse NI promote spontaneous locomotor activity and are activated in response to foot shock, a stimulus that elicits immediate locomotion. However, whether *Nmb* neurons are involved in the behavioral response to shock has not been directly tested. Through selective ablation of the NI *rln3a* or *gsc2* neurons we were able to assess whether each of these subtypes contributes to the observed changes in locomotion post-shock. We found that loss of either neuronal group was not sufficient to alter post-shock hyperactivity. Thus, if NI neurons play a role in the locomotor response to an acute aversive stimulus, their function may be redundant with other brain regions.

Neuronal activity following shock was not uniform across the NI; *gsc2* neurons exhibited a robust response to shock that was undetected in *rln3a* neurons. Moreover, we show that *gsc2* neurons receive input from the dHb-IPN pathway, which has been

implicated in regulating the behavioral response to aversive stimuli (Agetsuma et al., 2010; Duboué et al., 2017). A previous study reported that dHb neurons are activated several seconds after delivery of shock, and that more responsive neurons are located in the left dHb than the right. This lateralized activity is correlated with the resumption of swimming following freezing behavior exhibited by larvae post-shock (Duboué et al., 2017). However, given that the latency to respond to shock differs greatly between the dHb and *gsc2* neurons (17.5 ± 5.01 (Duboué et al., 2017) versus 3.14 ± 0.28 seconds), the response of *gsc2* neurons is not driven by the dHb and may serve a different role besides regulating locomotion, such as influencing fear memory formation (Szőnyi et al., 2019).

The IPN as an integrating center for dHb and NI input

Previous work demonstrated that axons from LdHb and RdHb neurons innervate different regions along the dorsoventral extent of the IPN; the LdHb neurons innervate the dIPN and vIPN whereas the RdHb neurons project mainly to the vIPN (Gamse et al., 2005). We found that different populations of NI neurons also target specific IPN compartments; *rln3a* neurons project mainly to the dIPN, whereas *gsc2* neurons predominantly innervate the vIPN along its midline neuropil. A recent study by Zaupa et al., 2021 demonstrated that axon terminals from cholinergic and noncholinergic dHb neurons, innervating the vIPN and dIPN respectively, have distinct patterns of activity. Spontaneous calcium spikes in cholinergic dHb terminals at the vIPN coincide with transient decreases in calcium signaling in dHb terminals at the dIPN. This negatively correlated activity was proposed to be mediated by activation of vIPN neurons that release GABA to inhibit non-cholinergic dHb terminals through their presynaptic $GABA_B$ receptors. The markedly different patterns of calcium signaling observed in dHb terminals innervating the vIPN and dIPN indicate that the two IPN subregions are differentially regulated by their dHb inputs. Our results, showing that *rln3a* and *gsc2* axons selectively terminate in the dIPN and vIPN, raise the possibility that innervation by different populations of NI neurons also shapes differential patterns of neural activity in the dorsal and ventral IPN. The IPN could thus integrate signals from disparate neuronal populations in the dHb and NI, and perhaps other brain regions. Future work

will determine whether *rln3a* and *gsc2* axon terminals exhibit distinct patterns of activity, and examine how their activity is coordinated with cholinergic and non-cholinergic dHb input to the dorsal and ventral IPN.

Toward understanding cell type heterogeneity in the NI

Overall, our study lays the foundation for a more holistic understanding of cell type heterogeneity in the NI. By mapping *gsc2, rln3a, nmbb,* and *cckb* neurons in the zebrafish NI, we found that *cckb* neurons are a separate population located posterior to the *rln3a* and *nmbb* neurons. Szlaga et al., 2022 also found little overlap between cholecystokinin and relaxin-3 neurons in the rat brain. The functional properties of cholecystokinin neurons in the NI are unknown. One study in zebrafish showed that overexpression of cholecystokinin increases waking locomotor activity (Woods et al., 2014). However, it is difficult to attribute this effect to Cholecystokinin neurons in any specific brain region because the neuropeptide was overexpressed globally. We also identified *nmbb* neurons in the PAG that are distinct from *rln3a* neurons and whose properties are unknown. The establishment of transgenic lines for selective labeling and manipulation of *cckb* and *nmbb* neurons, as we have demonstrated for *gsc2* and *rln3a*, will serve to further elucidate the connectivity and function of diverse neuronal populations in the NI and PAG. Ultimately, a more comprehensive view of NI and PAG cell type heterogeneity will advance our understanding of the neuroanatomical substrates that control arousal (Lu et al., 2020), fear (Szőnyi et al., 2019; Tovote et al., 2016), memory (Szőnyi et al., 2019; Ma et al., 2009), and feeding behaviors (McGowan et al., 2005).

ACKNOWLEDGEMENTS

We thank Dr. Bryan Luikart for sharing his expertise and equipment for two-photon microscopy, Jean-Michael Chanchu for generating *QUAS* transgenic lines, Essence Vinson and Ming Wu for assistance with *in situ* hybridization, Dr. Jeffrey Mumm for providing *he1.1:YFP* plasmid, and Dr. Rejji Kuruvilla and Dr. Erik Duboué for their valuable feedback on the manuscript. This work was supported by NIH R01HD078220,

R37HD091280 (M.E.H.) and a National Science Foundation Graduate Research Fellowship DGE-1746891 (E.D.S.).

AUTHOR CONTRIBUTIONS

Conceptualization: E.D.S. and M.E.H.; Data curation: E.D.S.; Formal analysis: E.D.S.; Funding acquisition: E.D.S. and M.E.H.; Investigation: E.D.S., A.S. and M.M.; Methodology: E.D.S., J.C. and M.M.; Project administration: M.E.H.; Resources: M.E.H.; Software: E.D.S.; Supervision: M.E.H.; Validation: E.D.S.; Visualization: E.D.S.; Writing – original draft: E.D.S.; Writing – review & editing: M.E.H and J.C.

DECLARATION OF INTERESTS

The authors declare no competing interests.

FIGURE LEGENDS

Figure 1. *gsc2* neurons localize to the nucleus incertus. (A, A') WISH for *gsc2* and (B-C') double-label WISH for (B, B') *gsc2* and *sst1.1* or (C, C') *gsc2* and *rln3a* was performed on (A-B') 4 dpf or (C, C') 6 dpf larvae. (A, C, C') Dorsal views. (A', B, B') Lateral views. (B', C') Enlarged views of boxed regions in B and C, respectively. Scale bars, 100 μm. (D-F) Fluorescent double-label WISH for (D) *rln3a* and *gsc2*, (E) *rln3a* and *nmbb*, and (F) *rln3a* and *cckb*. Dorsal views of 6 dpf larvae, Z-projections. Scale bar, 10 μm. (G) Schematic depicting distribution of neuronal subtypes in the larval zebrafish NI. Green dots, *gsc2* expression; purple dots, *rln3a* expression; blue dots, *nmbb* expression; pink dots and shading, *cckb* expression.

Figure 2. Transgenic driver lines recapitulate *gsc2* and *rln3a* expression patterns. (A, D) CRISPR/Cas9 genome editing strategies used to generate (A) *Tg(gsc2:QF2)*^{c721} and (D) *Tg(rln3a:QF2; he1.1:YFP)*^{c836} driver lines. (B, C, E, F) Dorsal views of 6 dpf larvae. (B, E) WISH for (B) *gsc2* and (E) *rln3a*. (C, F) Confocal Z-projections of (C) *Tg(gsc2:QF2)*^{c721}; *Tg(QUAS:GFP)*^{c578} and (F) *Tg(rln3a:QF2; he1.1:YFP)*^{c836}; *Tg(QUAS:GFP)*^{c578} larvae. Scale bars, 100 μm. sgRNA: single guide RNA, *hsp70*: *heat*

shock cognate 70-kd protein, tandem duplicate 1 promoter, 5' UTR: 5' untranslated region, HA: homology arm, he1.1: hatching enzyme promoter.

Figure 3. *rln3a* and *gsc2* NI neurons are largely GABAergic. (A-F'') Confocal images of 6 dpf larvae. (A-C) Z-projections, lateral views. (D-F'') Optical sections, dorsal views. (A) *Tg(gsc2:QF2)^{c721}*; *Tg(QUAS:GFP)^{c578}*; *Tg(slc17a6b:DsRed)^{nns9Tg}* larva. (B) PAG and (C) NI of a *Tg(rln3a:QF2; he1.1:YFP)^{c836}*; *Tg(QUAS:mApple; he1.1:CFP)^{c788}; Tg(slc17a6b:GFP)^{zf139Tg}* larva. (D, D') *Tg(gsc2:QF2)^{c721}*; *Tg(QUAS:mApple-CAAX; he1.1:mCherry)^{c636}*; *Tg(gad1b:GFP)^{nn25Tg}* larva. (D') Magnified view of boxed region in D. White arrowhead indicates a *gad1b*-positive *gsc2*-positive neuron. (E-F'') *Tg(rln3a:QF2; he1.1:YFP)^{c836}*; *Tg(QUAS:mApple; he1.1:CFP)^{c788}*; *Tg(gad1b:GFP)^{nn25Tg}* larva. (E-E'') View of PAG. (F-F'') View of NI. (E', F') Magnified views of boxed regions in E and F respectively. (E'', F'') Individual neurons indicated by arrowheads in E' and F' respectively. Top panels: GABAergic, middle panels: *rln3a*, bottom panels: composite. (G) Boxplot showing the percentage of *gsc2* and *rln3a* NI neurons, and *rln3a* PAG neurons that express *Tg(gad1b:GFP)^{nn25Tg}*, n = 3 larvae. Scale bars, 100 μm.

Figure 4. *gsc2* and *rln3a* neurons exhibit different projection patterns. (A-J) Confocal optical sections of (A-E) *Tg(gng8:Eco.NfsB-2A-CAAX-GFP)^{c375}*; Tg*(gsc2:QF2)^{c721}*; *Tg(QUAS:mApple-CAAX; he1.1:mCherry)^{c636}* and (F-J) *Tg(gng8:Eco.NfsB-2A-CAAX-GFP)^{c375}*; *Tg(rln3a:QF2; he1.1:YFP)^{c836}*; *Tg(QUAS:mApple-CAAX; he1.1:mCherry)^{c636}* 6 dpf larvae ordered from dorsal to ventral. (K-M) 3D reconstructions of confocal Z-stacks generated using Zen software (Zeiss), *Tg(rln3a:QF2; he1.1:YFP)^{c836}*; *Tg(QUAS:GFP-CAAX)^{c591}*; *Tg(QUAS:NLS-GFP; he1.1:CFP)^{c682}* larvae at 7 dpf showing efferents from (K) intact *rln3a* PAG (asterisks) and NI (arrows) neurons or following two-photon laser-mediated ablation of (L) PAG or (M) NI *rln3a* cell bodies at 6 dpf. Scale bars, 100 μm.

Figure 5. *gsc2* and *rln3a* NI neurons innervate different subregions of the IPN. (A-H') Confocal images of 6 dpf larvae. (A-B, E-F') *TgBAC(gng8:Eco.NfsB-2A-CAAX-GFP)^{c375}* and *Tg(gsc2:QF2)^{c721}* driving (A, A') *Tg(QUAS:NLS-mApple; he1.1:CFP)^{c718}* or

(B, E-F') *Tg(QUAS:mApple-CAAX; he1.1:mCherry)*^{c636}. (C-D, G-H') *TgBAC*(*gng8:GAL4FF*)^{c426}*; Tg(UAS-E1B:NTR-mCherry)*^{c264} and *Tg(rln3a:QF2; he1.1:YFP)*^{c836} driving (C, C') *Tg(QUAS:NLS-GFP; he1.1:CFP)*^{c682} or (D, G-H') *Tg(QUAS:NLS-GFP; he1.1:CFP)*^{c682} and *Tg(QUAS:GFP-CAAX)*^{c591}. (A', C') Higher magnification images of larvae in A and C, respectively. (A, A', C, C') Z-projections. (B, D) optical sections. (A-D) Lateral views. (E-H'') Dorsal views. Optical sections at the level of the (E, E', G, G') dorsal IPN or (F, F', H, H') ventral IPN of the same larvae. (E', F', G', H') Labeled efferent projections only. (I, J) Confocal Z-projections of coronal sections (70 μm) through adult brains of (I) *Tg(gsc2:QF2)*^{c721}; *Tg(QUAS:GFP-CAAX; he1.1:YFP)*^{c631} or (J) *Tg(rln3a:QF2; he1.1:YFP)*^{c836}; *Tg(QUAS:GFP-CAAX)*^{c591} fish. (K) Schematic of the IPN showing distinct regions innervated by *rln3a* and *gsc2* neurons. Scale bars, 100 μm.

Figure 6. Increased calcium signaling in *gsc2* neurons upon optogenetic activation of the dHb. Calcium transients were imaged at 2.6 Hz before, during, and after illumination with 561 nm light in 7 dpf larvae. (A) Drawings depicting imaging of calcium transients and optogenetic activation using confocal microscopy. (B-C') Representative maximum intensity projections of *GCaMP7a* fluorescence in (B, C) dHb and (B') *gsc2* or (C') *rln3a* NI neurons of the same larva. Scale bar, 100 μm. (D-E'') *Tg(gsc2:QF2)*^{c721} or (F-H'') *Tg(rln3a:QF2; he1.1:YFP)*^{c836} driver lines in (D-H) *TgBAC*(*gng8:GAL4FF*)^{c426}*; Tg(UAS:GCaMP7a)*^{zf415}; *Tg(QUAS:GCaMP7a)*^{c594} larvae (D, E, F, G, H) with *Tg(UAS:ReaChR-RFP)*^{if50} or (D', E', F', G', H') without. The average change in GCaMP7a signaling (%ΔF/F) is shown for (D, D', F, F') the dorsal habenulae, (E, E') *gsc2* neurons, (G, G') *rln3a* NI neurons, and (H, H') *rln3a* PAG neurons. Shading indicates standard deviation. Gaps at light onset and offset due to latency in switching laser configuration. (D'', E'', F'', G'', H'') Average F_{post}/F_{pre} is shown for (D'', F'') the dHb, (E'') *gsc2* neurons, (G'') *rln3a* NI neurons, and (H'') *rln3a* PAG neurons of *ReaChR*$^{+}$ and *ReaChR*$^{-}$ larvae (n=5 for each). F_{post} is the area under the curve for 15 frames during 561 nm illumination, and F_{pre} is the area under the curve for 15 frames preceding 561 nm illumination. Black bars indicate means. p values: Wilcoxon rank sum test. (D'') **p =

0.0043. (E'') **p = 0.0087. (F'') *p = 0.0317. (G'') p = 1. (H'') p = 0.6905. Extended y-axis in F'' to display higher values.

Figure 7. *gsc2* and *rln3a* NI neurons differ in spontaneous activity and response to electric shock. Calcium transients were imaged at 5.2 Hz in 7dpf larvae during a mild electric shock (25 V, 200 ms duration). (A) Drawing depicting delivery of shock to an immobilized larva during imaging. (B, C) Examples of maximum intensity projections for NI neurons in (B) *Tg(gsc2:QF2)^{c721}*; *Tg(QUAS:GCaMP7a)^{c594}* or (C) *Tg(rln3a:QF2; he1.1:YFP)^{c836}*; *Tg(QUAS:GCaMP7a)^{c594}* larvae. Scale bars, 10 μm. (D, E) Changes in *GCaMP7a* signaling (%ΔF/F) for representative individual (D) *gsc2* or (E) *rln3a* neurons. Arrows indicate local maxima identified as peaks by the MATLAB *findpeaks* function (MinPeakProminence: 0.3, MinPeakWidth: 10). (D', E') Average %ΔF/F for all recorded (D') *gsc2* neurons (93 from 11 larvae) or (E') *rln3a* neurons (76 from 10 larvae). Shading indicates standard deviation. (F) Average number of peaks during the recording period (as depicted by arrows in examples D and E) and (G) F_{post}/F_{pre} for *gsc2* neurons (n=11 larvae) and *rln3a* neurons (n=10 larvae). In G, F_{post} and F_{pre} are the area under the curve for 300 frames post-shock and for 300 frames prior to shock. (F, G) Black bars indicate means. p values: Wilcoxon rank sum test. (F) *p = 0.0124. (G) *p = 0.0265.

Figure 8. Loss of *rln3a* NI neurons increases spontaneous locomotor activity. (A-C''') Single optical sections from two-photon imaging of 6 dpf (A, A') *Tg(gsc2:QF2)^{c721}*; *Tg(QUAS:GFP)^{c578}* or (B-C''') *Tg(rln3a:QF2; he1.1:YFP)^{c836}*; *Tg(QUAS:GFP)^{c578}* larvae (A, B, C, C'') before and (A', B', C', C''') after laser-mediated ablation of (A, A') *gsc2* neurons, (B, B') *rln3a* NI neurons, or (C, C') left and (C'', C''') right *rln3a* PAG neurons. Scale bars, 10 μm. (D-D''') Representative movement trajectories of 7 dpf (D') *Tg(gsc2:QF2)^{c721}*; *Tg(QUAS:GFP)^{c578}* larvae with ablated *gsc2* neurons, (D'', D''') *Tg(rln3a:QF2; he1.1:YFP)^{c836}*; *Tg(QUAS:GFP)^{c578}* larvae with ablated (D'') *rln3a* NI neurons or (D''') *rln3a* PAG neurons, and (D) their sibling controls during the pre-shock period, defined as the first 115 seconds of the recording. Unablated control group includes *Tg(gsc2:QF2)^{c721}*; *Tg(QUAS:GFP)^{c578}* and *Tg(rln3a:QF2; he1.1:YFP)^{c836}*; *Tg(QUAS:GFP)^{c578}* larvae. (E) Total locomotor activity during the pre-shock period.

Unablated: n = 27 larvae, *gsc2* neurons ablated: n = 17 larvae, *rln3a* NI neurons ablated: n = 15 larvae, *rln3a* PAG neurons ablated: n = 17 larvae. Kruskal-Wallis rank sum test: p = 0.0009853***. Dunn's post-hoc tests with adjustment for multiple comparisons: *rln3a* NI neurons ablated vs. unablated p = 0.0019**, *rln3a* NI neurons ablated vs. *gsc2* neurons ablated p = 0.0019**, or *rln3a* NI neurons ablated vs. *rln3a* PAG neurons ablated p = 0.0019**. (F) Average bout length during the pre-shock period, with bouts defined as continuous periods of movement and no more than one second of prolonged immobility. Kruskal-Wallis rank sum test: p = 0.001344**. Dunn's post-hoc tests with adjustment for multiple comparisons: *rln3a* NI neurons ablated vs. unablated p = 0.03884*, *rln3a* NI neurons ablated vs. *gsc2* neurons ablated p = 0.03884*, or *rln3a* NI neurons ablated vs. *rln3a* PAG neurons ablated p = 0.00055***. (G) Bout number during the pre-shock period. Kruskal-Wallis rank sum test: p = 0.8895. (H-H''') Average locomotor activity during 5 seconds prior to and 5 seconds post-shock plotted for groups shown in D-D'''. Shock delivery is denoted by the gray line. (I) Total locomotor activity during 5 seconds pre-shock, and 5 seconds post-shock. Kruskal-Wallis rank sum test: 2.2×10^{-16}. Dunn's post-hoc tests with adjustment for multiple comparisons: no statistically significant differences within pre-shock and post-shock groups, p < 0.001*** for each pre-shock vs. post-shock comparison.

TABLES

Table 1. Properties of *gsc2* and *rln3a* NI neurons.

	Neurotransmitter identity	Afferents from IPN	Efferents to IPN	Spontaneous activity	Response to shock	Locomotion post-ablation
***gsc2* neurons**	0% *vglut2a*$^+$ 82.43± 3.52% *gad1b*$^+$	Yes	Ventral IPN	Low spontaneous activity	Robust activation	No change
***rln3a* NI neurons**	0% *vglut2a*$^+$ 80.57± 5.57% *gad1b*$^+$	No	Dorsal IPN	Rhythmic calcium bursts	Lack of response	Increased

STAR METHODS

Resource availability

Lead contact

Requests for further information, resources, and reagents should be directed to and will be fulfilled by the lead contact, Dr. Marnie Halpern (Marnie.E.Halpern@dartmouth.edu).

Materials Availability

Plasmids generated in this study have been deposited to Addgene. Plasmid numbers are listed in the key resources table.

Data and Code Availability

All data reported in this paper will be shared by the lead contact upon request. All original code has been deposited at Zenodo and is publicly available as of the date of publication. DOIs are listed in the key resources table. Any additional information required to reanalyze the data reported in this paper is available from the lead contact upon request.

Experimental model and subject details

Zebrafish were maintained at 27 °C in a 14:10 h light/dark cycle in a recirculating system with dechlorinated water (system water). The AB wild-type strain (Walker, 1998) was used along with the following transgenic lines: *TgBAC(gng8:Eco.NfsB-2A-CAAX-GFP)*^{c375} (described previously (deCarvalho et al., 2013)), *Tg(gsc2:QF2)*^{c721}, *Tg(rln3a:QF2; he1.1:YFP)*^{c836}, *Tg(QUAS:GFP)*^{c578}, *Tg(slc17a6b:DsRed)*^{nns9Tg} (described previously (Miyasaka et al., 2009)), *Tg(QUAS:mApple; he1.1:CFP)*^{c788}, *Tg(slc17a6b:EGFP)*^{zf139Tg} (described previously (Miyasaka et al., 2009)), *Tg(QUAS:mApple-CAAX; he1.1:mCherry)*^{c636} (described previously (Choi et al., 2021)), *Tg(gad1b:GFP)*^{nn25Tg} (described previously (Satou et al., 2013)), *Tg(QUAS:GFP-CAAX)*^{c591}, *TgBAC*(*gng8:GAL4FF*)^{c426} (described previously (Hong et al., 2013)), *Tg(UAS-E1B:NTR-mCherry)*^{c264} (described previously (Davison et al., 2007)),

675 *Tg(QUAS:NLS-mApple; he1.1:CFP)^{c718}*, *Tg(QUAS:NLS-GFP; he1.1:CFP)^{c682}*,
676 *Tg(QUAS:GFP-CAAX; he1.1:YFP)^{c631}*, *Tg(UAS:GCaMP7a)^{zf415}* (described previously
677 (Muto et al., 2013)), *Tg(QUAS:GCaMP7a)^{c594}*, and *Tg(UAS:ReaChR-RFP)^{jf50}* (described
678 previously (Wee et al., 2019)). Fluorescent larvae were screened using an Olympus
679 MVX10 Macro Zoom Fluorescence microscope. For imaging, larvae were incubated in
680 system water containing 0.003% phenylthiourea (PTU; P7629, Sigma-Aldrich) to inhibit
681 melanin pigmentation. Most analyses were performed at the larval stage, before sex
682 determination. Analyses performed at the adult stage included both males and females.
683 All zebrafish protocols were approved by the Institutional Animal Care and Use
684 Committee (IACUC) of the Carnegie Institution for Science or Dartmouth College.

685 **Method details**

686 *Generation of transgenic lines by Tol2 transgenesis*
687 To generate *Tg(QUAS:GFP)^{c578}*, *Tg(QUAS:mApple; he1.1:CFP)^{c788}*, *Tg(QUAS:GFP-*
688 *CAAX)^{c591}*, *Tg(QUAS:NLS-mApple; he1.1:CFP)^{c718}*, *Tg(QUAS:NLS-GFP;*
689 *he1.1:CFP)^{c682}*, *Tg(QUAS:GFP-CAAX; he1.1:YFP)^{c631}* and *Tg(QUAS:GCaMP7a)^{c594}*
690 transgenic lines, constructs for Tol2 transposition were created using the MultiSite
691 Gateway-based construction kit (Kwan et al., 2007). For each construct, three entry
692 vectors were first assembled by BP reactions (11789020, Thermo Fisher Scientific). A
693 16 bp *QUAS* sequence (Potter et al., 2010) was cloned into the 5' entry vector
694 (*pDONRP4-P1R*, #219 of Tol2kit v1.2). DNA encoding *GFP*, *mApple*, *GFP-CAAX*, *NLS*
695 *(nuclear localization sequence)-mApple* or *NLS-GFP* was cloned into middle entry
696 vectors (*pDONR221*, #218 of Tol2kit v1.2). Sequences corresponding to the *SV40 poly*
697 *A* tail, or the *poly A* tail followed by a secondary marker consisting of the
698 zebrafish *hatching enzyme 1, tandem duplicate 1* (*he1.1*) promoter (Xie et al., 2012)
699 driving CFP (cyan fluorescent protein) or YFP (yellow fluorescent protein), were cloned
700 into the 3' entry vector (*pDONRP2R-P3*, #220 of Tol2kit v1.2). All three entry vectors
701 were introduced into a Tol2 destination construct (*pDestTol2pA2*, #394 of the Tol2kit
702 v1.2) using an LR reaction (11791020, Thermo Fisher Scientific).
703 To produce Tol2 transposase mRNA, *pCS-zT2TP* (Suster et al., 2009) was
704 digested with *Not*I and RNA was synthesized *in vitro* using the mMESSAGE

mMACHINE Transcription Kit with SP6 polymerase (AM1340, Thermo Fisher Scientific). RNA was extracted with phenol/chloroform-isoamyl alcohol, re-extracted with chloroform, and precipitated with isopropanol. A solution containing *QUAS* plasmid DNA (25 ng/µl), Tol2 transposase mRNA (25 ng/µl) and phenol red (0.5%) was microinjected into one-cell stage zebrafish embryos. Founders were identified by screening progeny for fluorescent hatching gland cells at 1 dpf or *QUAS*-driven expression.

Generation of transgenic lines by genome editing

Methods for CRISPR/Cas9-targeted integration were used to generate the *Tg(gsc2:QF2)*^{c721} and *Tg(rln3a:QF2; he1.1:YFP)*^{c836} driver lines. For *Tg(gsc2:QF2)*^{c721}, the non-homologous end joining approach described by Kimura et al., 2014 was modified by using a *QF2* donor plasmid, *Gbait-hsp70-QF2-pA* (Addgene plasmid #122563), which contains a GFP bait sequence for Cas9-mediated linearization of the plasmid (Choi et al., 2021). Cas9 RNA and sgRNAs targeting *gsc2* and the GFP bait sequence were synthesized using a previously described approach (Hwang et al., 2013; Jao et al., 2013; Auer et al., 2014). Briefly, pairs of synthetic oligonucleotides (*gsc2*_sense, 5'TAGGTCACCGCACCATCTTCACAG3', *gsc2*_anti-sense 5'AACCTGTGAAGATGGTGCGGTGA3'), containing the overhangs 5'-TAGG-N_{18}-3' and 5'-AAAC-N_{18}-3', were annealed to each other. The resulting DNA was cloned into the *pDR274* vector (Addgene, plasmid #42250; Hwang et al., 2013) following digestion of *pDR274* with *Bsa*I (R3733S, New England Biolabs). The *pDR274* vector for synthesis of the GFP bait sgRNA was provided Dr. Filippo Del Bene (Auer et al., 2014). *pDR274* templates were digested by *Dra*I and sgRNAs synthesized using the MAXIscript T7 Transcription Kit (AM1312, Thermo Fisher Scientific). *pT3TS-nCas9n* template DNA (Addgene, plasmid #46757; Jao et al., 2013) was digested with *Xba*I (R0145S, New England Biolabs), and Cas9 RNA was synthesized using the mMESSAGE mMACHINE Transcription Kit (AM1348, Fisher Scientific). A solution containing *gsc2* sgRNA (50 ng/µl), GFP bait sgRNA (50 ng/µl), the *Gbait-hsp70-QF2-pA* plasmid (50 ng/µl), Cas9 mRNA (500 ng/µl), and phenol red (0.5%) was microinjected into one-cell stage embryos.

For *Tg(rln3a:QF2; he1.1:YFP)*^{c836}, the GeneWeld approach described by Wierson et al., 2020, which uses short homology arms to facilitate integration by homology-directed repair, was modified by introduction of *QF2* into the donor vector. The resulting *pPRISM-QF2-he1.1:YFP* donor construct contains two target sites for a universal sgRNA (ugRNA), which flank the cargo: a 2A self-cleaving sequence, *QF2*, and the *he1.1:YFP* secondary marker. To generate the construct, four PCR products were produced. *QF2* was amplified from *Gbait-hsp70-QF2-pA* (Addgene plasmid #122563; Choi et al., 2021) (2A_*QF2*_F: 5'AAACCCCGGTCCTATGCCACCCAAGCGCAAA3', 2A_*QF2*_R: 5'TTAATTACTAGTTTCACTGTTCGTATGTATTAATGTCGGAG3'). The *he1.1:YFP* cassette (Addgene, plasmid #113879) was amplified from DNA provided by Dr. Jeffrey Mumm (*he1.1:YFP*_F: 5'TAGTTCTTTAAACTCAACCACTCCAGGCATAGC3', *he1.1:YFP*_R: 5'TCCGCCTCAGAAGCCATAGAGCCCACCGCATC3'), and the polyA terminator (polyA_F: 5'TACGAACAGTGAAACTAGTAATTAAGTCTCAGCCAC3', polyA_R: 5'TGGAGTGGTTGAGTTTAAAGAACTAGGAACGCC3') and plasmid backbone (Col1E_F: 5'TGGGCTCTATGGCTTCTGAGGCGGAAAGAAC3', Col1E_R: 5'CTTGGGTGGCATAGGACCGGGGTTTTCTTC3') were amplified from *pPRISM-Stop-cmlc2-eGFP* (Addgene kit #1000000154; Wierson et al., 2020) which was provided by Dr. Maura McGrail. The PCR-amplified fragments were assembled using NEBuilder HiFi DNA Assembly Cloning Kit (E5520S, New England Biosystems).

To generate *rln3a* homology arms, complementary oligonucleotide pairs (*rln3a*_5'arm_sense: 5'GCGGTTTCTCGGCTCTCGTAGTGTGTCTGCTGCTGGCTGGAGTAAAGGCGCTGGAC3', *rln3a*_5'arm_anti-sense: 5'GAAGGTCCAGCGCCTTTACTCCAGCCAGCAGCAGACACACTACGAGAGCCGAGAAA3', *rln3a*_3'arm_sense: 5'CGGTTTCGGATGAACTCCCTGCCGCATAATTTGACTCCATACGAGGGCCCGGCG3', *rln3a*_3'arm_anti-sense: 5'AAGCGCCGGGCCCTCGTATGGAGTCAAATTATGCGGCAGGGAGTTCATCCGAAA3') were designed using GTagHD (Wierson et al., 2020) and annealed to each other. To clone the homology arms into the *pPRISM-QF2-he1.1:YFP* donor vector*, pPRISM-QF2-he1.1:YFP* was first digested with *Bfu*AI and *Bsp*QI, (R0701S and R0712S, New England Biolabs) then combined with the homology arms in a ligation reaction (M0202S, New England Biolabs). To synthesize ugRNA and an sgRNA targeting the *rln3a* gene, synthetic oligonucleotide pairs (*rln3a*_sense:

5'TAATACGACTCACTATAGGAGTAAAGGCGCTGGACGCGTTTTAGAGCTAGAAATA GC3', ugRNA_sense: 5'TAATACGACTCACTATAGGGAGGCGTTCGGGCCACAGGTT TTAGAGCTAGAAATAGC3', common_anti-sense: 5'AAAAGCACCGACTCGGTGCCAC TTTTTCAAGTTGATAACGGACTAGCCTTATTTTAACTTGCTATTTCTAGCTCTAAAAC 3') were annealed to each other, elongated using Phusion polymerase (M0530S, New England Biolabs), and used as templates for *in vitro* transcription with the MAXIscript T7 Transcription Kit (AM1312, Thermo Fisher Scientific). A solution containing *rln3a* sgRNA (50 ng/µl), universal sgRNA (50 ng/µl), the *pPRISM-QF2-he1.1:YFP-rln3a-HA* plasmid (100 ng/µl), Cas9 mRNA (500 ng/µl), and phenol red (0.5%) was microinjected into one-cell stage embryos.

To verify successful integration, PCR was performed on genomic DNA from injected embryos using primers that flank the integration site, with the forward primer corresponding to genomic sequence and the reverse primer corresponding to plasmid sequence (*gsc2*_F: 5'GTC TGGGGAAAGCGTGTGTT3', *hsp70*_R: 5'TCAAGTCGCTTCTCTTCGGT3'; *rln3a*_F: 5'CGCTTTTGTTTCCAGAAAGG3', *QF2*_R: 5'CAGACCCGGAGTATCGATGT3'). Sanger sequencing confirmed identity of PCR products. Transgenic founders were identified by breeding F_0 adults with a *QUAS* reporter line and screening progeny for *QUAS*-driven expression. PCR and sequencing were repeated in F_1 larvae to confirm integration at the target site.

RNA in situ hybridization

DNA templates for *gsc2*, *rln3a*, *ccka* and *cckb* probes were generated using PCR to incorporate a binding site for SP6 polymerase. cDNA for PCR amplification was obtained by reverse transcription of RNA extracted from 6 dpf embryos with TRIzol (15596026, Invitrogen) using the QuantiTect Reverse Transcription kit (205311, Qiagen). PCR primer sequences were: *gsc2*_F: 5'GTGCAGGACAAGAGGAGCTT3', *gsc2*_R: 5'GTTTCAATTTAGGTGACACTATAGTCCTCGAAGACTGAAGGGAA3', rln3a_F: 5'CACAGATGAAATCCTGGACTTGT3', *rln3a*_R: 5'GTTTCAATTTAGGTGACACTATAGCTGAAATGAGAGAGCGAGCA3', *ccka*_F: 5'TCTGTGTATGTGCCCTGCTG3', *ccka*_R: 5'GTTTCAATTTAGGTGACACTATAGTG

GCCAGTAGTTCGGTTAGG3'; *cckb*_F: 5'GGGGTGTGTGTGTGTGTGAT3', *cckb*_R: 5'GTTTCAATTTAGGTGACACTAGAGATGAGTTTGGCCAGCAG3'. DNA templates for *nmba*, *nmbb* and *nts* were amplified from cDNA (*nmba*_F: 5'ATGGCTGATGATGGACATTG3', *nmba*_R: 5'CATCCTGTTGGCCAATTCTT3'; *nmbb*_F: 5'CAGTCCAAGCGTATCCAGGT3', *nmbb*_R: 5'TCATTTATTGTCTTGAATGT AGCTTT3'; *nts*_F: 5'TTGTGTGTTTTCTCCCTCTTCA3', *nts*_R: 5'CGGCCGTCTGGAT TTATTAG3'), cloned using the TOPO TA kit (K465001, Invitrogen), and linearized by digestion with *BamH*I (R0136S, New England Biolabs). The template for the *sst1.1* probe was an *sst1.1* clone in a *pSPORT1* vector (from Dr. Joshua Gamse) linearized by digestion with *Sal*I (R3138L, New England Biolabs).

DNA templates were used for digoxigenin (DIG)-labeled *in vitro* transcription of *gsc2*, *rln3a*, *ccka*, *cckb*, *nmba*, *nmbb,* and *nts* probes (11175025910, Roche) and fluorescein (FITC)-labeled *in vitro* transcription of *rln3a* and *sst1.1* probes (11685619910, Roche). The *gsc2*, *rln3a*, *ccka*, *cckb* and *sst1.1* probes were synthesized with SP6 polymerase and the *nmba*, *nmbb*, and *nts* probes were synthesized with T7 polymerase (Fisher Scientific, EP0113). Probes were purified using illustra MicroSpin G-50 Columns (27533001, GE Healthcare).

RNA *in situ* hybridization was performed as previously described (Thisse et al., 1993; Liang et al., 2000). Larvae and dissected adult brains were fixed overnight in paraformaldehyde (PFA; 4% in 1x phosphate-buffered saline) at 4°C then dehydrated overnight in 100% methanol (A4124, Fisher Scientific) at -20°C. Tissue was rehydrated stepwise in methanol/PBS and washed with PBT (1x PBS, 0.1% Tween 20). Larvae were digested for 30 minutes and adult brains for 35 minutes in proteinase K (3115836001, Roche; 10 µg/ml in PBT). To stop the reaction, tissue was fixed in 4% PFA at room temperature for 20 minutes, then washed with PBT. Tissue was prehybridized for at least two hours at 70°C in hybridization buffer [50% formamide (17899, Fisher Scientific), 5X saline sodium citrate (SSC), 50 µg/ml heparin (H3393, Sigma-Aldrich), 500 µg/ml tRNA (10109525001, Sigma-Aldrich), 0.1% Tween 20 (P1379, Sigma-Aldrich), 9 mM citric acid] with 5% dextran and then hybridized overnight at 70°C in hybridization buffer with dextran and 30 ng of probe. Samples were then washed in hybridization buffer (without dextran), transitioned stepwise at 70°C from

hybridization buffer to 2X SSC, washed twice for 30 minutes in 0.2x SSC at 70°C, and transitioned stepwise into PBT at room temperature. Adult brains were embedded in 4% low melting point agarose (50100, Lonza) and sectioned using a Leica VT1000s vibratome. Whole mount larvae and adult brain sections were blocked for at least one hour in PBT with 2 mg/ml BSA (bovine serum albumin) and 2% sheep serum and incubated overnight at 4°C with alkaline phosphatase-coupled anti-DIG antiserum (11093274910, Roche) diluted 1/5000 in blocking solution. Samples were washed several times in PBT, and detection with 4-Nitro blue tetrazolium chloride (NBT) (11383213001, Roche) and 5-bromo-4-chloro-3-indolyl-phosphate (BCIP) (11383221001, Roche) was performed in alkaline phosphatase reaction buffer [100 mM Tris pH 9.5, 50 mM $MgCl_2$, 100 mM NaCl, 0.1% Tween 20].

For colorimetric double *in situ* hybridization (Liang et al., 2000), larvae were hybridized with DIG and FITC probes simultaneously, and the DIG probe was first detected using NBT/BCIP as described above. To inactivate alkaline phosphatase, larvae were post-fixed overnight at room temperature in 4% PFA, washed twice for 20 minutes each with MABT [100 mM maleic acid, 150 mM NaCl, 0.1% Tween-20, pH 7.5], incubated for 10 minutes at 70°C in EDTA (10 mM in MABT), and dehydrated in methanol for 10 minutes. Samples were rehydrated stepwise in methanol/MABT, washed in MABT, and blocked for 1 hour in blocking buffer: 20% sheep serum and 2% blocking reagent (11096176001, Roche) in MABT. Tissue was incubated overnight at 4°C in alkaline phosphatase-coupled anti-FITC antiserum (11426338910, Roche) diluted 1:5000 in blocking buffer. Finally, samples were washed several times in MABT, and FITC detection with BCIP and iodo-nitrotetrazolium violet was performed in alkaline phosphatase buffer with 10% polyvinyl alcohol. Following *in situ* hybridization, samples were cleared in glycerol and mounted for imaging with a Zeiss Axioskop microscope fitted with a Leica DFC 500 digital color camera using Leica Applications Suite software.

For fluorescent double *in situ* hybridization, larvae were fixed in 4% PFA, dehydrated in methanol, and incubated in 2% hydrogen peroxide in methanol for 20 minutes. After rehydration and washing in PBT as above, larvae were digested for 30 minutes in 20 µg/ml proteinase K in PBT, post-fixed in 4% PFA, washed, prehybridized as above, and hybridized overnight at 70°C in hybridization buffer with 5% dextran and

40 ng each of DIG and FITC probes. Stringency washes were performed as above, then larvae were washed in TNT [0.1M Tris pH 7.5, 0.1M NaCl, 0.1% Tween-20] and maintained for 2 hours in 2% blocking reagent (11096176001, Roche) in TNT. Larvae were incubated overnight at 4°C in horseradish peroxidase-coupled anti-FITC antiserum (11426346910, Roche) diluted 1:500 in blocking solution, then washed several times in TNT. FITC detection was performed using TSA Plus fluorescein diluted 1:50 in amplification diluent (NEL741001KT, Akoya Biosciences). Samples were washed several times in TNT, incubated in 1% hydrogen peroxide in TNT for 20 minutes, washed again in TNT, blocked as above for 1 hour, and incubated overnight at 4°C in horseradish peroxidase-coupled anti-DIG antiserum (11207733910, Roche) diluted 1:500 in blocking solution. Tissue was washed several more times in TNT and DIG detection was performed using TSA Plus Cyanine diluted 1:50 in amplification diluent (NEL744001KT, Akoya Biosciences).

DiI labeling

Brains were dissected from *TgBAC(gng8:Eco.NfsB-2A-CAAX-GFP)*^{c375} adult zebrafish euthanized by exposure to 4° C water for 10 minutes. Brains were fixed in 4% PFA overnight at 4° C, rinsed in 1x PBS, and mounted in 4% low melting point agarose (50100, Lonza). Using a Leica VT1000s vibratome, 70 µm sections were removed, starting from the forebrain and sectioning posteriorly until the IPN was visible. Using GFP-labeled dHb axon terminals as a reference, DiI (N22880, Invitrogen) was applied to the exposed dorsal IPN using the tip of a tungsten needle under an Olympus MVX10 Macro Zoom Fluorescence microscope. The labeled hemibrains were incubated at 27° C for either 3 or 5 days and, after incubation, sectioned in 70 µm slices for confocal imaging.

Confocal imaging

Larvae were anesthetized in 0.02% tricaine and individually mounted in a droplet of 1.5% low melting point agarose (50100, Lonza) centered in a 60 mm x 15 mm Petri dish. After the agarose solidified, system water with 0.02% tricaine was added to each

dish. Larvae were imaged using a Leica SP5 with a 25X (NA = 0.95) water immersion objective, or a Zeiss LSM 980 with a 20X (NA=0.5) water immersion objective.

Adult brains were fixed overnight in 4% PFA at 4°C, rinsed in 1x PBS, and mounted in 4% low melting point agarose (50100, Lonza) for sectioning using a Leica VT1000s vibratome. Sections were mounted in glycerol for imaging using a Leica SP5 with a 20X (NA = 0.7) objective, or a Zeiss LSM 980 with a 20X (NA=0.8) objective.

Calcium imaging

Larvae were paralyzed by a 1 minute immersion in α-bungarotoxin (20 µl of 1 mg/ml solution in system water, B1601, ThermoFisher Scientific) followed by washing in fresh system water (Duboué et al., 2017; Baraban, 2013; Severi et al., 2014). Each larva was embedded in a droplet of 1.5% low melting point agarose (50100, Lonza) centered in a 60 mm x 15 mm Petri dish. After the agarose solidified, system water was added to each dish. For all calcium imaging experiments, images were acquired in *xyt* acquisition mode using a Zeiss LSM 980 with a 20X (NA=0.5) water immersion objective.

To record calcium transients in response to electric shock, a PVC ring holding electrodes which were connected to a Grass SD9 electrical stimulator (Grass Instruments), was placed in each dish (Duboué et al., 2017). Images of *gsc2* or *rln3a* NI neurons were acquired using a 488 nm laser at 475 x 475 pixel resolution and a rate of 5.2 Hz. Calcium transients were recorded for 600 frames, larvae were shocked once (25V, 200 msec duration; Duboué et al., 2017) and 1800 more frames were collected.

To record calcium transients in response to stimulation with 561 nm light, images were acquired using a 488 nm laser at 310 x 310 pixel resolution and a rate of 2.6 Hz. The Z-depth was adjusted to the plane of the neuronal population being imaged (i.e. dHb, PAG or NI). Spontaneous calcium transients were recorded for 200 frames, the 561 nm laser was activated while 20 more frames were acquired, and then calcium transients were recorded for another 150 frames.

For all calcium imaging experiments, image frames were extracted in Fiji (Schindelin et al., 2012) using *File -> Save As -> Separate Image Files*. Image frames were imported to MATLAB, and mean fluorescence intensities for regions of interest (ROI) were calculated. Briefly, for each larva a high contrast image was generated by

calculating a maximum intensity projection of its image series. ROIs were drawn manually using the high contrast image and the MATLAB function *roipoly*. For recordings of *gsc2* and *rln3a* neurons, ROIs were individual neurons; for dHb recordings, each dHb nucleus was an ROI. Mean fluorescence intensity of pixels within each ROI was calculated. Finally, ΔF/F (Vogelstein et al., 2010; Duboué et al., 2017) was calculated according to the following formula:

$$F \leftarrow \frac{F_i - F_{min}}{F_{max} - F_{min}}$$

where F_i indicates the mean fluorescence intensity in an ROI at each time point, and F_{max} and F_{min} are the maximum and minimum fluorescence values respectively for that ROI during the recording period. To calculate total activity for each larva before and after the stimulus, ΔF/F was averaged across all ROIs in each larva and total activity was obtained for time period by calculating the area under the curve using the MATLAB function *trapz*.

Two-photon-mediated laser ablation

At 6 dpf, *Tg(gsc2:QF2)*^{c721}; *Tg(QUAS:GFP)*^{c578} or *Tg(rln3a:QF2; he1.1:YFP)*^{c836}; *Tg(QUAS:GFP)*^{c578} larvae were anesthetized in 0.02% tricaine and individually mounted in a droplet of 1.5% low melting point agarose (50100, Lonza) centered in a 30 mm x 10 mm Petri dish. After the agarose solidified, system water was added. GFP-expressing cells were located using a two-photon microscope (Bruker) with a 60X (NA = 1) objective. The laser was tuned to 885 nm and using GFP labeling as a guide, was focused on the relevant cell population and activated for several seconds at maximum power until the GFP signal disappeared. Because the two-photon laser power is delivered to a restricted Z-plane, ablations were repeated at multiple Z-depths to eliminate each cell population. For *gsc2* neuron ablation, the laser was activated over an area of 600-2000 um^2 on each of four Z-planes. For *rln3a* NI neuron ablation, the laser was activated over an area of 1000-1250 um^2 on each of two Z-planes. For ablation of each *rln3a* PAG nucleus (left and right), the laser was activated over an area

of 1200-1800 um^2 on each of two Z-planes. For unablated controls, GFP-expressing neurons were located on the same microscope but were not exposed to the laser at maximum power.

Locomotor Assay

Behavioral experiments were performed blind to the ablation status of the larva being assayed. Unablated controls were a mix of *Tg(gsc2:QF2)*^{c721}; *Tg(QUAS:GFP)*^{c578} and *Tg(rln3a:QF2; he1.1:YFP)*^{c836}; *Tg(QUAS:GFP)*^{c578}, and were siblings of ablated larvae. Behavioral tests were conducted in a temperature-controlled room (27° C) on 7 dpf larvae. The 6 cm^3 acrylic testing chamber had a 0.5 cm platform, on top of which a 40 mm cell strainer (Falcon) was placed. The chamber was filled with fresh system water and set on top of an infrared illumination source (880 nm, ViewPoint Life Sciences). Locomotor activity was recorded by a high frame rate charged couple device (CCD) camera (Point Grey Research), which was connected to a computer (Dell). Tracking was performed in real time at 60 frames per second, using ZebraLab software (ViewPoint Life Sciences). Swimming behavior was recorded for 120 seconds, then each larva was shocked once (25 V, 200 ms duration) and activity recorded for an additional 120 seconds. To analyze locomotor activity, the x and y coordinates of a larva's position in each frame were exported from ZebraLab. Activity was quantified using R statistical software according to the following equation:

$$D = \sqrt{(x_{i+1} - x_i)^2 + (y_{i+1} - y_i)^2}$$

where i indicates a single frame. Total distances were calculated by summing the distance for each frame over the relevant period of the recording. Total number of movement bouts and average length of movement bouts during the pre-shock period were calculated for each larva using R statistical software. Movement trajectories were plotted using MATLAB.

Quantification and statistical analysis

All means are presented with standard error of the mean. Statistical details for all experiments can be found in the figure legends. Analyses were nonparametric and were performed using either R statistical software or MATLAB. The Wilcoxon rank sum test was used for comparisons between two groups, and the Kruskal-Wallis test was used for comparisons between multiple groups. When the Kruskal-Wallis test reached a threshold of $p < 0.05$, the Dunn's post-hoc test with correction for multiple comparisons was performed. Sample sizes were similar to those typically used in zebrafish behavior and calcium imaging studies (Agetsuma et al., 2010; Facchin et al., 2015; Duboué et al., 2017; Wee et al., 2019; Muto et al., 2013; Choi et al., 2021). Data were plotted using the MATLAB library PlotPub (K M Masum Habib, 2022) or the R package ggplot2 (Hadley Wickham, 2016).

Key resources table

See attached document

SUPPLEMENTAL INFORMATION LEGENDS

Supplementary Figure 1. Subset of neuropeptides expressed in larval zebrafish NI. WISH for (A-A') *ccka*, (B-B') *cckb*, (C-C') *nmba*, (D-D') *nmbb*, or (E-E') *nts* in 6 dpf larvae. Dorsal views of the same larvae were imaged at (A, B, C, D, E) dorsal and (A', B', C', D', E') ventral planes. White arrowheads indicate NI. Scale bar, 100 μm.

Supplementary Figure 2. Overlapping expression of *rln3a* and *nmbb* in the zebrafish NI. Fluorescent double-label WISH for *rln3a* and *nmbb.* Dorsal views of 6 dpf larvae. (A) Z-projection and (A'-A''') higher magnification image of NI from larva in A. (B-C'') NI in two additional larvae. (A'-C'') Optical sections showing (A', B, C) *rln3a* neurons, (A'', B', C') *nmbb* neurons, and (A''', B'', C'') composite images. White arrowheads indicate neurons that co-express *rln3a* and *nmbb*. (A) Scale bar, 100 μm. (A'-C'') Scale bar, 10 μm.

Supplementary Figure 3. QF2 driver lines recapitulate *gsc2* and *rln3a* expression patterns in the adult brain. (A) Schematic lateral view of adult zebrafish brain (after Wullimann et al., 1996), indicating positions of coronal sections (70 µm) shown in (B-G). (B, D, F) WISH for (B) *gsc2* and (D, F) *rln3a*. (C, E, G) Confocal Z-projections of labeled neurons in (C) *Tg(gsc2:QF2)*^{c721}; *Tg(QUAS:GFP)*^{c578} and (E, G) *Tg(rln3a:QF2; he1.1:YFP)*^{c836}; *Tg(QUAS:GFP)*^{c578} brains. Scale bars, 100 µm.

Supplementary Figure 4. Axons from the dIPN terminate at *gsc2* NI neurons. (A-C') Confocal Z-projections of 70 µm coronal vibratome sections of adult *Tg(gsc2:QF2)*^{c721}; *Tg(QUAS:GFP)*^{c578}; *Tg(gng8:Eco.NfsB-2A-CAAX-GFP)*^{c375} brains. (A-C) Three examples of DiI labeling (white arrowheads) at the application site in the IPN and (A'-C') of efferent fibers at the NI of the same brain. Brains sectioned after (A, A') 3 or (B-C') 5 days of incubation at 27° C. Scale bars, 100 µm.

Supplementary Figure 5. Confirmation of selective ablation of NI neuronal clusters. (A-D') WISH for (A, A', C, C') *gsc2* or (B, B', D, D') *rln3a* was performed on 7 dpf larvae. (A', B') *Tg(gsc2:QF2)*^{c721}; *Tg(QUAS:GFP)*^{c578} larvae whose *gsc2* neurons were ablated at 6 dpf. (C', D') *Tg(rln3a:QF2; he1.1:YFP)*^{c836}; *Tg(QUAS:GFP)*^{c578} larvae whose *rln3a* NI neurons were ablated at 6 dpf. (A, B, C, D) Unablated sibling controls for larvae in A', B', C' and D' respectively.

Supplementary Video 1. Axonal projections of *gsc2* neurons. Rotating 3D reconstruction of a 6 dpf *Tg(gng8:Eco.NfsB-2A-CAAX-GFP)*^{c375}; Tg*(gsc2:QF2)*^{c721}; *Tg(QUAS:mApple-CAAX; he1.1:mCherry)*^{c636} larva generated using a Zeiss LSM 980 and Zen software.

Supplementary Video 2. Axonal projections of *rln3a* neurons. Rotating 3D reconstruction of a 6 dpf *Tg(gng8:Eco.NfsB-2A-CAAX-GFP)*^{c375}; *Tg(rln3a:QF2; he1.1:YFP)*^{c836}; *Tg(QUAS:mApple-CAAX; he1.1:mCherry)*^{c636} larva generated using a Zeiss LSM 980 and Zen software.

Supplementary Video 3. Axonal projections of *rln3a* neurons after ablation of *rln3a* PAG cell bodies. Rotating 3D reconstruction of a 7 dpf *Tg(rln3a:QF2; he1.1:YFP)^{c836}*; *Tg(QUAS:GFP-CAAX)^{c591}*; *Tg(QUAS:NLS-GFP; he1.1:CFP)^{c682}* larva whose *rln3a* PAG neurons were ablated at 6 dpf, showing the pronounced projections from the *rln3a* NI neurons to the IPN. Generated using a Zeiss LSM 980 and Zen software.

Supplementary Video 4. Calcium transients in *gsc2* neurons. Calcium transients in the *gsc2* neurons of a 7 dpf *Tg(gsc2:QF2)^{c721}*; *Tg(QUAS:GCaMP7a)^{c594}* larva during the delivery of an electric shock (25 V, 200 ms duration), which is denoted by text in upper left corner. Calcium transients imaged at 5.2 Hz. Video sped up 3X.

Supplementary Video 5. Calcium transients in *rln3a* neurons. Calcium transients in the *rln3a* neurons in the NI of a 7 dpf *Tg(rln3a:QF2; he1.1:YFP)^{c836}*; *Tg(QUAS:GCaMP7a)^{c594}* larva during the delivery of an electric shock (25 V, 200 ms duration), which is denoted by text in upper left corner. Calcium transients imaged at 5.2 Hz. Video sped up 3X.

Supplementary Video 6. Increased locomotor behavior upon loss of *rln3a* NI neurons. Freely swimming 7 dpf larvae. Left: Unablated control larva. Right: Larva whose *rln3a* NI neurons were ablated at 6 dpf. Red dot marks the position of the larva for ease of tracking. Larvae were removed from 1x phenylthiourea at 6 dpf after two-photon ablation protocol to allow for the development of pigment, which increases visibility.

REFERENCES

Agetsuma, M., Aizawa, H., Aoki, T., Nakayama, R., Takahoko, M., Goto, M., Sassa, T., Amo, R., Shiraki, T., Kawakami, K., et al. (2010). The habenula is crucial for experience-dependent modification of fear responses in zebrafish. Nat. Neurosci. *13*, 1354–1356. https://doi.org/10.1038/nn.2654.

Ahumada-Galleguillos, P., Lemus, C.G., Díaz, E., Osorio-Reich, M., Härtel, S., and Concha, M.L. (2017). Directional asymmetry in the volume of the human habenula. Brain Struct. Funct. *222*, 1087–1092. https://doi.org/10.1007/s00429-016-1231-z.

1072 Albus, M. (1988). Cholecystokinin. Prog. Neuropsychopharmacol. Biol. Psychiatry *12*,
1073 S5–S21. https://doi.org/10.1016/0278-5846(88)90071-1.

1074 Auer, T.O., Duroure, K., De Cian, A., Concordet, J.-P., and Del Bene, F. (2014). Highly
1075 efficient CRISPR/Cas9-mediated knock-in in zebrafish by homology-independent DNA
1076 repair. Genome Res. *24*, 142–153. https://doi.org/10.1101/gr.161638.113.

1077 Baraban, S.C. (2013). Forebrain electrophysiological recording in larval zebrafish. J.
1078 Vis. Exp. JoVE 50104. https://doi.org/10.3791/50104.

1079 Bittencourt, J.C., and Sawchenko, P.E. (2000). Do centrally administered neuropeptides
1080 access cognate receptors?: an analysis in the central corticotropin-releasing factor
1081 system. J. Neurosci. Off. J. Soc. Neurosci. *20*, 1142–1156. .

1082 Burazin, T.C.D., Bathgate, R.A.D., Macris, M., Layfield, S., Gundlach, A.L., and
1083 Tregear, G.W. (2002). Restricted, but abundant, expression of the novel rat gene-3 (R3)
1084 relaxin in the dorsal tegmental region of brain. J. Neurochem. *82*, 1553–1557.
1085 https://doi.org/10.1046/j.1471-4159.2002.01114.x.

1086 Choi, J.-H., Duboue, E.R., Macurak, M., Chanchu, J.-M., and Halpern, M.E. (2021).
1087 Specialized neurons in the right habenula mediate response to aversive olfactory cues.
1088 ELife *10*, e72345. https://doi.org/10.7554/eLife.72345.

1089 Davison, J.M., Akitake, C.M., Goll, M.G., Rhee, J.M., Gosse, N., Baier, H., Halpern,
1090 M.E., Leach, S.D., and Parsons, M.J. (2007). Transactivation from Gal4-VP16
1091 transgenic insertions for tissue-specific cell labeling and ablation in zebrafish. Dev. Biol.
1092 *304*, 811–824. https://doi.org/10.1016/j.ydbio.2007.01.033.

1093 deCarvalho, T.N., Akitake, C.M., Thisse, C., Thisse, B., and Halpern, M.E. (2013).
1094 Aversive cues fail to activate fos expression in the asymmetric olfactory-habenula
1095 pathway of zebrafish. Front. Neural Circuits *7*, 98.
1096 https://doi.org/10.3389/fncir.2013.00098.

1097 deCarvalho, T.N., Subedi, A., Rock, J., Harfe, B.D., Thisse, C., Thisse, B., Halpern,
1098 M.E., and Hong, E. (2014). Neurotransmitter map of the asymmetric dorsal habenular
1099 nuclei of zebrafish. Genes. N. Y. N 2000 *52*, 636–655.
1100 https://doi.org/10.1002/dvg.22785.

1101 Doll, C.A., Burkart, J.T., Hope, K.D., Halpern, M.E., and Gamse, J.T. (2011).
1102 Subnuclear development of the zebrafish habenular nuclei requires ER translocon
1103 function. Dev. Biol. *360*, 44–57. https://doi.org/10.1016/j.ydbio.2011.09.003.

1104 Donizetti, A., Grossi, M., Pariante, P., D'Aniello, E., Izzo, G., Minucci, S., and Aniello, F.
1105 (2008). Two neuron clusters in the stem of postembryonic zebrafish brain specifically
1106 express relaxin-3 gene: first evidence of nucleus incertus in fish. Dev. Dyn. Off. Publ.
1107 Am. Assoc. Anat. *237*, 3864–3869. https://doi.org/10.1002/dvdy.21786.

1108 Donizetti, A., Fiengo, M., Minucci, S., and Aniello, F. (2009). Duplicated zebrafish
1109 relaxin-3 gene shows a different expression pattern from that of the co-orthologue gene.
1110 Dev. Growth Differ. *51*, 715–722. https://doi.org/10.1111/j.1440-169X.2009.01131.x.

1111 Duboué, E.R., Hong, E., Eldred, K.C., and Halpern, M.E. (2017). Left Habenular Activity
1112 Attenuates Fear Responses in Larval Zebrafish. Curr. Biol. CB *27*, 2154-2162.e3.
1113 https://doi.org/10.1016/j.cub.2017.06.017.

1114 Facchin, L., Duboué, E.R., and Halpern, M.E. (2015). Disruption of Epithalamic Left-
1115 Right Asymmetry Increases Anxiety in Zebrafish. J. Neurosci. Off. J. Soc. Neurosci. *35*,
1116 15847–15859. https://doi.org/10.1523/JNEUROSCI.2593-15.2015.

1117 Farooq, U., Kumar, J.R., Rajkumar, R., and Dawe, G.S. (2016). Electrical
1118 microstimulation of the nucleus incertus induces forward locomotion and rotation in rats.
1119 Physiol. Behav. *160*, 50–58. https://doi.org/10.1016/j.physbeh.2016.03.033.

1120 Funato, H., Sato, M., Sinton, C.M., Gautron, L., Williams, S.C., Skach, A., Elmquist,
1121 J.K., Skoultchi, A.I., and Yanagisawa, M. (2010). Loss of Goosecoid-like and DiGeorge
1122 syndrome critical region 14 in interpeduncular nucleus results in altered regulation of
1123 rapid eye movement sleep. Proc. Natl. Acad. Sci. U. S. A. *107*, 18155–18160.
1124 https://doi.org/10.1073/pnas.1012764107.

1125 Gamse, J.T., Kuan, Y.-S., Macurak, M., Brösamle, C., Thisse, B., Thisse, C., and
1126 Halpern, M.E. (2005). Directional asymmetry of the zebrafish epithalamus guides
1127 dorsoventral innervation of the midbrain target. Dev. Camb. Engl. *132*, 4869–4881.
1128 https://doi.org/10.1242/dev.02046.

1129 Gong, S., Zheng, C., Doughty, M.L., Losos, K., Didkovsky, N., Schambra, U.B., Nowak,
1130 N.J., Joyner, A., Leblanc, G., Hatten, M.E., et al. (2003). A gene expression atlas of the
1131 central nervous system based on bacterial artificial chromosomes. Nature *425*, 917–
1132 925. https://doi.org/10.1038/nature02033.

1133 Goto, M., Swanson, L.W., and Canteras, N.S. (2001). Connections of the nucleus
1134 incertus. J. Comp. Neurol. *438*, 86–122. .

1135 Gottlieb, S., Hanes, S.D., Golden, J.A., Oakey, R.J., and Budarf, M.L. (1998).
1136 Goosecoid-like, a gene deleted in DiGeorge and velocardiofacial syndromes,
1137 recognizes DNA with a bicoid-like specificity and is expressed in the developing mouse
1138 brain. Hum. Mol. Genet. *7*, 1497–1505. https://doi.org/10.1093/hmg/7.9.1497.

1139 Hadley Wickham (2016). ggplot2: Elegant Graphics for Data Analysis. (New York:
1140 Springer-Verlag).

1141 Harris, J.A., Guglielmotti, V., and Bentivoglio, M. (1996). Diencephalic asymmetries.
1142 Neurosci. Biobehav. Rev. *20*, 637–643. .

1143 Hong, E., Santhakumar, K., Akitake, C.A., Ahn, S.J., Thisse, C., Thisse, B., Wyart, C.,
1144 Mangin, J.-M., and Halpern, M.E. (2013). Cholinergic left-right asymmetry in the

habenulo-interpeduncular pathway. Proc. Natl. Acad. Sci. U. S. A. *110*, 21171–21176. https://doi.org/10.1073/pnas.1319566110.

Hosken, I.T., Sutton, S.W., Smith, C.M., and Gundlach, A.L. (2015). Relaxin-3 receptor (Rxfp3) gene knockout mice display reduced running wheel activity: Implications for role of relaxin-3/RXFP3 signalling in sustained arousal. Behav. Brain Res. *278*, 167–175. https://doi.org/10.1016/j.bbr.2014.09.028.

Hwang, W.Y., Fu, Y., Reyon, D., Maeder, M.L., Tsai, S.Q., Sander, J.D., Peterson, R.T., Yeh, J.-R.J., and Joung, J.K. (2013). Efficient genome editing in zebrafish using a CRISPR-Cas system. Nat. Biotechnol. *31*, 227–229. https://doi.org/10.1038/nbt.2501.

Jao, L.-E., Wente, S.R., and Chen, W. (2013). Efficient multiplex biallelic zebrafish genome editing using a CRISPR nuclease system. Proc. Natl. Acad. Sci. *110*, 13904–13909. https://doi.org/10.1073/pnas.1308335110.

Jennes, L., Stumpf, W.E., and Kalivas, P.W. (1982). Neurotensin: Topographical distribution in rat brain by immunohistochemistry. J. Comp. Neurol. *210*, 211–224. https://doi.org/10.1002/cne.902100302.

K M Masum Habib (2022). PlotPub - Publication Quality Graphs in MATLAB.

Kimura, Y., Hisano, Y., Kawahara, A., and Higashijima, S. (2014). Efficient generation of knock-in transgenic zebrafish carrying reporter/driver genes by CRISPR/Cas9-mediated genome engineering. Sci. Rep. *4*, 6545. https://doi.org/10.1038/srep06545.

Kubota, Y., Inagaki, S., Shiosaka, S., Cho, H.J., Tateishi, K., Hashimura, E., Hamaoka, T., and Tohyama, M. (1983). The distribution of cholecystokinin octapeptide-like structures in the lower brain stem of the rat: An immunohistochemical analysis. Neuroscience *9*, 587–604. https://doi.org/10.1016/0306-4522(83)90176-8.

Kwan, K.M., Fujimoto, E., Grabher, C., Mangum, B.D., Hardy, M.E., Campbell, D.S., Parant, J.M., Yost, H.J., Kanki, J.P., and Chien, C.-B. (2007). The Tol2kit: A multisite gateway-based construction kit forTol2 transposon transgenesis constructs. Dev. Dyn. *236*, 3088–3099. https://doi.org/10.1002/dvdy.21343.

Lawther, A.J., Clissold, M.L., Ma, S., Kent, S., Lowry, C.A., Gundlach, A.L., and Hale, M.W. (2015). Anxiogenic drug administration and elevated plus-maze exposure in rats activate populations of relaxin-3 neurons in the nucleus incertus and serotonergic neurons in the dorsal raphe nucleus. Neuroscience *303*, 270–284. https://doi.org/10.1016/j.neuroscience.2015.06.052.

Liang, J.O., Etheridge, A., Hantsoo, L., Rubinstein, A.L., Nowak, S.J., Izpisúa Belmonte, J.C., and Halpern, M.E. (2000). Asymmetric nodal signaling in the zebrafish diencephalon positions the pineal organ. Dev. Camb. Engl. *127*, 5101–5112. .

1180 Lin, J.Y., Knutsen, P.M., Muller, A., Kleinfeld, D., and Tsien, R.Y. (2013). ReaChR: a
1181 red-shifted variant of channelrhodopsin enables deep transcranial optogenetic
1182 excitation. Nat. Neurosci. *16*, 1499–1508. https://doi.org/10.1038/nn.3502.

1183 Lu, L., Ren, Y., Yu, T., Liu, Z., Wang, S., Tan, L., Zeng, J., Feng, Q., Lin, R., Liu, Y., et
1184 al. (2020). Control of locomotor speed, arousal, and hippocampal theta rhythms by the
1185 nucleus incertus. Nat. Commun. *11*, 262. https://doi.org/10.1038/s41467-019-14116-y.

1186 Ma, S., and Gundlach, A.L. (2015). Ascending Control of Arousal and Motivation: Role
1187 of Nucleus Incertus and its Peptide Neuromodulators in Behavioural Responses to
1188 Stress. J. Neuroendocrinol. *27*, 457–467. https://doi.org/10.1111/jne.12259.

1189 Ma, S., Bonaventure, P., Ferraro, T., Shen, P.-J., Burazin, T.C.D., Bathgate, R. a. D.,
1190 Liu, C., Tregear, G.W., Sutton, S.W., and Gundlach, A.L. (2007). Relaxin-3 in GABA
1191 projection neurons of nucleus incertus suggests widespread influence on forebrain
1192 circuits via G-protein-coupled receptor-135 in the rat. Neuroscience *144*, 165–190.
1193 https://doi.org/10.1016/j.neuroscience.2006.08.072.

1194 Ma, S., Olucha-Bordonau, F.E., Hossain, M.A., Lin, F., Kuei, C., Liu, C., Wade, J.D.,
1195 Sutton, S.W., Nuñez, A., and Gundlach, A.L. (2009). Modulation of hippocampal theta
1196 oscillations and spatial memory by relaxin-3 neurons of the nucleus incertus. Learn.
1197 Mem. *16*, 730–742. https://doi.org/10.1101/lm.1438109.

1198 Ma, S., Blasiak, A., Olucha-Bordonau, F.E., Verberne, A.J.M., and Gundlach, A.L.
1199 (2013). Heterogeneous responses of nucleus incertus neurons to corticotrophin-
1200 releasing factor and coherent activity with hippocampal theta rhythm in the rat. J.
1201 Physiol. *591*, 3981–4001. https://doi.org/10.1113/jphysiol.2013.254300.

1202 Ma, S., Smith, C.M., Blasiak, A., and Gundlach, A.L. (2017). Distribution, physiology
1203 and pharmacology of relaxin-3/RXFP3 systems in brain: Relaxin-3/RXFP3 systems in
1204 brain. Br. J. Pharmacol. *174*, 1034–1048. https://doi.org/10.1111/bph.13659.

1205 McGowan, B.M.C., Stanley, S.A., Smith, K.L., White, N.E., Connolly, M.M., Thompson,
1206 E.L., Gardiner, J.V., Murphy, K.G., Ghatei, M.A., and Bloom, S.R. (2005). Central
1207 Relaxin-3 Administration Causes Hyperphagia in Male Wistar Rats. Endocrinology *146*,
1208 3295–3300. https://doi.org/10.1210/en.2004-1532.

1209 McLaughlin, I., Dani, J.A., and De Biasi, M. (2017). The medial habenula and
1210 interpeduncular nucleus circuitry is critical in addiction, anxiety, and mood regulation. J.
1211 Neurochem. *142 Suppl 2*, 130–143. https://doi.org/10.1111/jnc.14008.

1212 Miyasaka, N., Morimoto, K., Tsubokawa, T., Higashijima, S. -i., Okamoto, H., and
1213 Yoshihara, Y. (2009). From the Olfactory Bulb to Higher Brain Centers: Genetic
1214 Visualization of Secondary Olfactory Pathways in Zebrafish. J. Neurosci. *29*, 4756–
1215 4767. https://doi.org/10.1523/JNEUROSCI.0118-09.2009.

Muto, A., Ohkura, M., Abe, G., Nakai, J., and Kawakami, K. (2013). Real-Time Visualization of Neuronal Activity during Perception. Curr. Biol. *23*, 307–311. https://doi.org/10.1016/j.cub.2012.12.040.

Nasirova, N., Quina, L.A., Morton, G., Walker, A., and Turner, E.E. (2020). Mapping Cell Types and Efferent Pathways in the Ascending Relaxin-3 System of the Nucleus Incertus. Eneuro *7*, ENEURO.0272-20.2020. https://doi.org/10.1523/ENEURO.0272-20.2020.

Nuñez, A., Cervera-Ferri, A., Olucha-Bordonau, F., Ruiz-Torner, A., and Teruel, V. (2006). Nucleus incertus contribution to hippocampal theta rhythm generation. Eur. J. Neurosci. *23*, 2731–2738. https://doi.org/10.1111/j.1460-9568.2006.04797.x.

Ohki-Hamazaki, H. (2000). Neuromedin B. Prog. Neurobiol. *62*, 297–312. https://doi.org/10.1016/S0301-0082(00)00004-6.

Olson, I., Suryanarayana, S.M., Robertson, B., and Grillner, S. (2017). Griseum centrale, a homologue of the periaqueductal gray in the lamprey. IBRO Rep. *2*, 24–30. https://doi.org/10.1016/j.ibror.2017.01.001.

Olucha-Bordonau, F.E., Teruel, V., Barcia-González, J., Ruiz-Torner, A., Valverde-Navarro, A.A., and Martínez-Soriano, F. (2003). Cytoarchitecture and efferent projections of the nucleus incertus of the rat. J. Comp. Neurol. *464*, 62–97. https://doi.org/10.1002/cne.10774.

Olucha-Bordonau, F.E., Albert-Gascó, H., Ros-Bernal, F., Rytova, V., Ong-Pålsson, E.K.E., Ma, S., Sánchez-Pérez, A.M., and Gundlach, A.L. (2018). Modulation of forebrain function by nucleus incertus and relaxin-3/RXFP3 signaling. CNS Neurosci. Ther. *24*, 694–702. https://doi.org/10.1111/cns.12862.

Palva, J.M., and Palva, S. (2012). Infra-slow fluctuations in electrophysiological recordings, blood-oxygenation-level-dependent signals, and psychophysical time series. NeuroImage *62*, 2201–2211. https://doi.org/10.1016/j.neuroimage.2012.02.060.

Passerin, A.M., Cano, G., Rabin, B.S., Delano, B.A., Napier, J.L., and Sved, A.F. (2000). Role of locus coeruleus in foot shock-evoked Fos expression in rat brain. Neuroscience *101*, 1071–1082. .

Potter, C.J., Tasic, B., Russler, E.V., Liang, L., and Luo, L. (2010). The Q System: A Repressible Binary System for Transgene Expression, Lineage Tracing, and Mosaic Analysis. Cell *141*, 536–548. https://doi.org/10.1016/j.cell.2010.02.025.

Potter, E., Sutton, S., Donaldson, C., Chen, R., Perrin, M., Lewis, K., Sawchenko, P.E., and Vale, W. (1994). Distribution of corticotropin-releasing factor receptor mRNA expression in the rat brain and pituitary. Proc. Natl. Acad. Sci. U. S. A. *91*, 8777–8781. .

R Core Team R: A language and environment for statistical computing. (Vienna, Austria: R Foundation for Statistical Computing).

1253 Rajkumar, R., Wu, Y., Farooq, U., Tan, W.H., and Dawe, G.S. (2016). Stress activates
1254 the nucleus incertus and modulates plasticity in the hippocampo-medial prefrontal
1255 cortical pathway. Brain Res. Bull. *120*, 83–89.
1256 https://doi.org/10.1016/j.brainresbull.2015.10.010.

1257 Riabinina, O., and Potter, C.J. (2016). The Q-System: A Versatile Expression System
1258 for Drosophila. Methods Mol. Biol. Clifton NJ *1478*, 53–78. https://doi.org/10.1007/978-
1259 1-4939-6371-3_3.

1260 Ryan, P.J., Büchler, E., Shabanpoor, F., Hossain, M.A., Wade, J.D., Lawrence, A.J.,
1261 and Gundlach, A.L. (2013). Central relaxin-3 receptor (RXFP3) activation decreases
1262 anxiety- and depressive-like behaviours in the rat. Behav. Brain Res. *244*, 142–151.
1263 https://doi.org/10.1016/j.bbr.2013.01.034.

1264 Ryczko, D., and Dubuc, R. (2017). Dopamine and the Brainstem Locomotor Networks:
1265 From Lamprey to Human. Front. Neurosci. *11*, 295.
1266 https://doi.org/10.3389/fnins.2017.00295.

1267 Saint-Jore, B., Puech, A., Heyer, J., Lin, Q., Raine, C., Kucherlapati, R., and Skoultchi,
1268 A.I. (1998). Goosecoid-like (GSCL), a candidate gene for velocardiofacial syndrome, is
1269 not essential for normal mouse development. Hum. Mol. Genet. *7*, 1841–1849.
1270 https://doi.org/10.1093/hmg/7.12.1841.

1271 Satou, C., Kimura, Y., Hirata, H., Suster, M.L., Kawakami, K., and Higashijima, S.
1272 (2013). Transgenic tools to characterize neuronal properties of discrete populations of
1273 zebrafish neurons. Dev. Camb. Engl. *140*, 3927–3931.
1274 https://doi.org/10.1242/dev.099531.

1275 Schindelin, J., Arganda-Carreras, I., Frise, E., Kaynig, V., Longair, M., Pietzsch, T.,
1276 Preibisch, S., Rueden, C., Saalfeld, S., Schmid, B., et al. (2012). Fiji: an open-source
1277 platform for biological-image analysis. Nat. Methods *9*, 676–682.
1278 https://doi.org/10.1038/nmeth.2019.

1279 Severi, K.E., Portugues, R., Marques, J.C., O'Malley, D.M., Orger, M.B., and Engert, F.
1280 (2014). Neural control and modulation of swimming speed in the larval zebrafish.
1281 Neuron *83*, 692–707. https://doi.org/10.1016/j.neuron.2014.06.032.

1282 Smith, C.M., Shen, P.-J., Banerjee, A., Bonaventure, P., Ma, S., Bathgate, R.A.D.,
1283 Sutton, S.W., and Gundlach, A.L. (2010). Distribution of relaxin-3 and RXFP3 within
1284 arousal, stress, affective, and cognitive circuits of mouse brain. J. Comp. Neurol. *518*,
1285 4016–4045. https://doi.org/10.1002/cne.22442.

1286 Smith, C.M., Ryan, P.J., Hosken, I.T., Ma, S., and Gundlach, A.L. (2011). Relaxin-3
1287 systems in the brain--the first 10 years. J. Chem. Neuroanat. *42*, 262–275.
1288 https://doi.org/10.1016/j.jchemneu.2011.05.013.

Smith, C.M., Hosken, I.T., Sutton, S.W., Lawrence, A.J., and Gundlach, A.L. (2012). Relaxin-3 null mutation mice display a circadian hypoactivity phenotype. Genes Brain Behav. *11*, 94–104. https://doi.org/10.1111/j.1601-183X.2011.00730.x.

Streeter, G.L. (1903). Anatomy of the floor of the fourth ventricle. (The relations between the surface markings and the underlying structures.). Am. J. Anat. *2*, 299–313. https://doi.org/10.1002/aja.1000020303.

Subedi, A., Macurak, M., Gee, S.T., Monge, E., Goll, M.G., Potter, C.J., Parsons, M.J., and Halpern, M.E. (2014). Adoption of the Q transcriptional regulatory system for zebrafish transgenesis. Methods San Diego Calif *66*, 433–440. https://doi.org/10.1016/j.ymeth.2013.06.012.

Suster, M.L., Sumiyama, K., and Kawakami, K. (2009). Transposon-mediated BAC transgenesis in zebrafish and mice. BMC Genomics *10*, 477. https://doi.org/10.1186/1471-2164-10-477.

Szlaga, A., Sambak, P., Trenk, A., Gugula, A., Singleton, C.E., Drwiega, G., Blasiak, T., Ma, S., Gundlach, A.L., and Blasiak, A. (2022). Functional Neuroanatomy of the Rat Nucleus Incertus–Medial Septum Tract: Implications for the Cell-Specific Control of the Septohippocampal Pathway. Front. Cell. Neurosci. *16*, 836116. https://doi.org/10.3389/fncel.2022.836116.

Szőnyi, A., Sos, K.E., Nyilas, R., Schlingloff, D., Domonkos, A., Takács, V.T., Pósfai, B., Hegedüs, P., Priestley, J.B., Gundlach, A.L., et al. (2019). Brainstem nucleus incertus controls contextual memory formation. Science *364*, eaaw0445. https://doi.org/10.1126/science.aaw0445.

Tanaka, M., Iijima, N., Miyamoto, Y., Fukusumi, S., Itoh, Y., Ozawa, H., and Ibata, Y. (2005). Neurons expressing relaxin 3/INSL 7 in the nucleus incertus respond to stress. Eur. J. Neurosci. *21*, 1659–1670. https://doi.org/10.1111/j.1460-9568.2005.03980.x.

Thirumalai, V., and Cline, H.T. (2008). Endogenous Dopamine Suppresses Initiation of Swimming in Prefeeding Zebrafish Larvae. J. Neurophysiol. *100*, 1635–1648. https://doi.org/10.1152/jn.90568.2008.

Thisse, C., Thisse, B., Schilling, T.F., and Postlethwait, J.H. (1993). Structure of the zebrafish snail1 gene and its expression in wild-type, spadetail and no tail mutant embryos. Dev. Camb. Engl. *119*, 1203–1215. .

Tovote, P., Esposito, M.S., Botta, P., Chaudun, F., Fadok, J.P., Markovic, M., Wolff, S.B.E., Ramakrishnan, C., Fenno, L., Deisseroth, K., et al. (2016). Midbrain circuits for defensive behaviour. Nature *534*, 206–212. https://doi.org/10.1038/nature17996.

Vogelstein, J.T., Packer, A.M., Machado, T.A., Sippy, T., Babadi, B., Yuste, R., and Paninski, L. (2010). Fast nonnegative deconvolution for spike train inference from population calcium imaging. J. Neurophysiol. *104*, 3691–3704. https://doi.org/10.1152/jn.01073.2009.

Walker, C. (1998). Chapter 3 Haploid Screens and Gamma-Ray Mutagenesis. In Methods in Cell Biology, (Elsevier), pp. 43–70.

Wee, C.L., Song, E.Y., Johnson, R.E., Ailani, D., Randlett, O., Kim, J.-Y., Nikitchenko, M., Bahl, A., Yang, C.-T., Ahrens, M.B., et al. (2019). A bidirectional network for appetite control in larval zebrafish. ELife *8*. https://doi.org/10.7554/eLife.43775.

Wierson, W.A., Welker, J.M., Almeida, M.P., Mann, C.M., Webster, D.A., Torrie, M.E., Weiss, T.J., Kambakam, S., Vollbrecht, M.K., Lan, M., et al. (2020). Efficient targeted integration directed by short homology in zebrafish and mammalian cells. ELife *9*. https://doi.org/10.7554/eLife.53968.

Woods, I.G., Schoppik, D., Shi, V.J., Zimmerman, S., Coleman, H.A., Greenwood, J., Soucy, E.R., and Schier, A.F. (2014). Neuropeptidergic Signaling Partitions Arousal Behaviors in Zebrafish. J. Neurosci. *34*, 3142–3160. https://doi.org/10.1523/JNEUROSCI.3529-13.2014.

Wullimann, M.F., Rupp, B., and Reichert, H. (1996). Neuroanatomy of the Zebrafish Brain (Basel: Birkhäuser Basel).

Xie, X., Mathias, J.R., Smith, M.-A., Walker, S.L., Teng, Y., Distel, M., Köster, R.W., Sirotkin, H.I., Saxena, M.T., and Mumm, J.S. (2012). Silencer-delimited transgenesis: NRSE/RE1 sequences promote neural-specific transgene expression in a NRSF/REST-dependent manner. BMC Biol. *10*, 93. https://doi.org/10.1186/1741-7007-10-93.

Zaupa, M., Naini, S.M.A., Younes, M.A., Bullier, E., Duboué, E.R., Le Corronc, H., Soula, H., Wolf, S., Candelier, R., Legendre, P., et al. (2021). Trans-inhibition of axon terminals underlies competition in the habenulo-interpeduncular pathway. Curr. Biol. *31*, 4762-4772.e5. https://doi.org/10.1016/j.cub.2021.08.051.

Zhang, C., Chua, B.E., Yang, A., Shabanpoor, F., Hossain, M.A., Wade, J.D., Rosengren, K.J., Smith, C.M., and Gundlach, A.L. (2015). Central relaxin-3 receptor (RXFP3) activation reduces elevated, but not basal, anxiety-like behaviour in C57BL/6J mice. Behav. Brain Res. *292*, 125–132. https://doi.org/10.1016/j.bbr.2015.06.010.

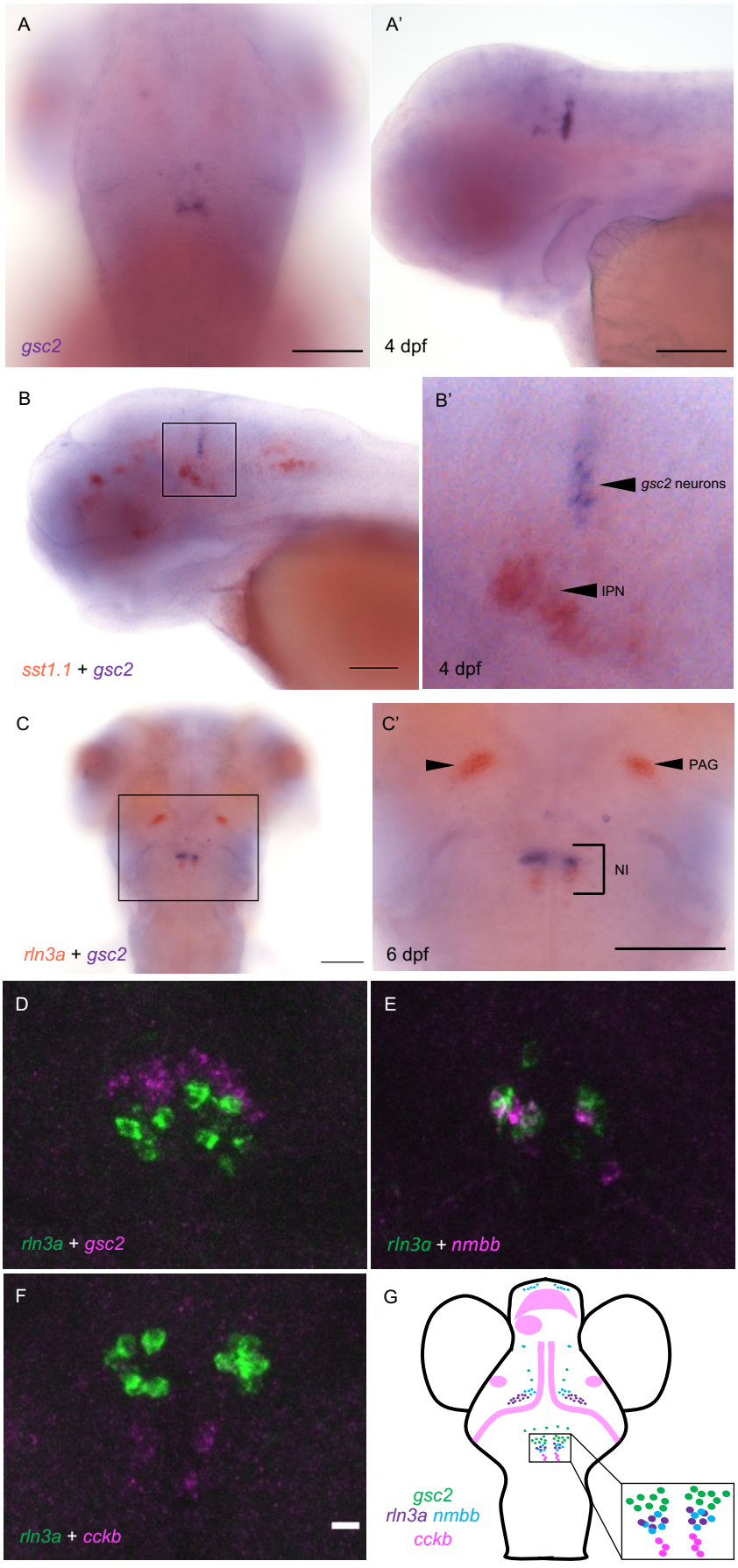

Figure 2

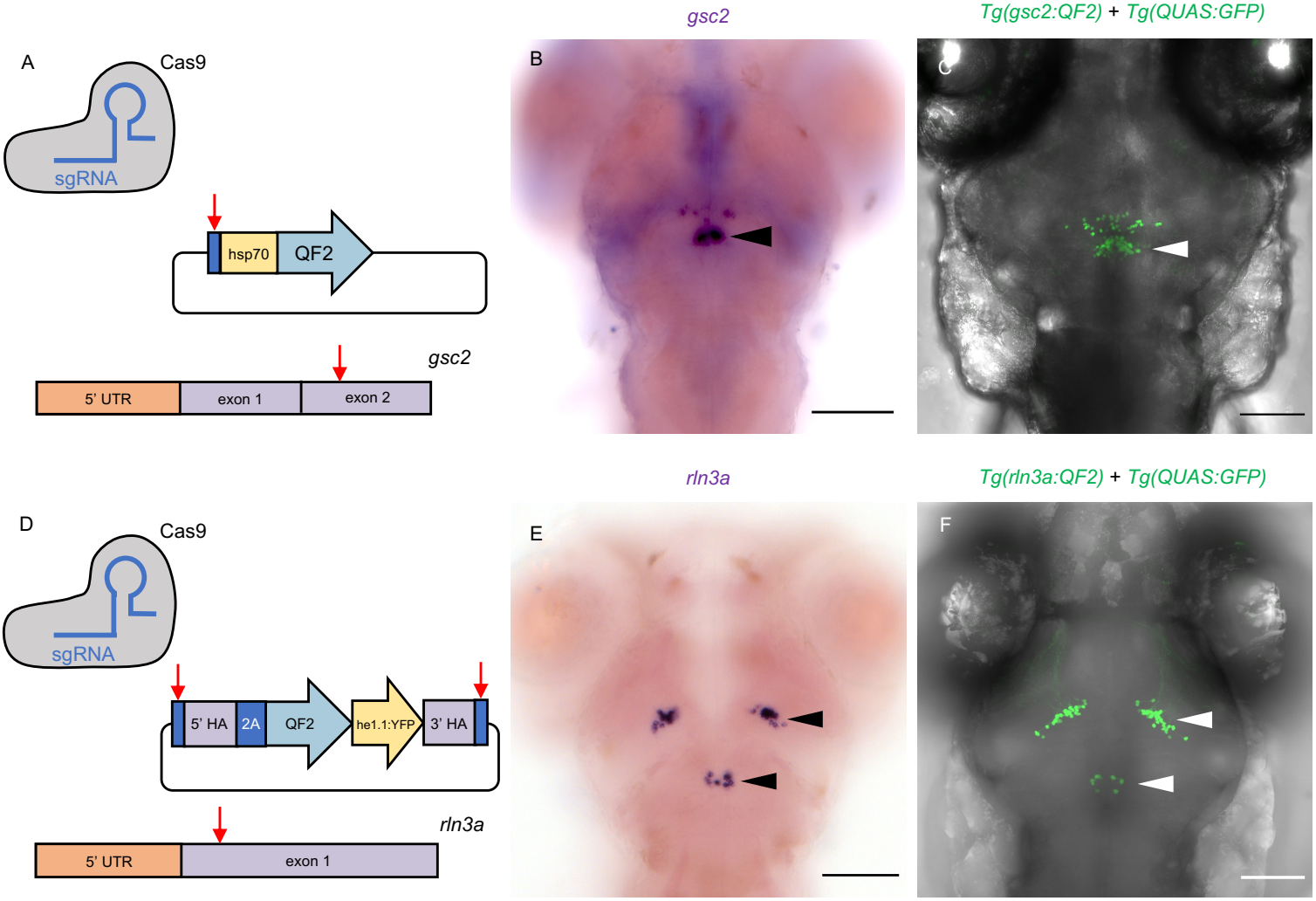

Figure 3

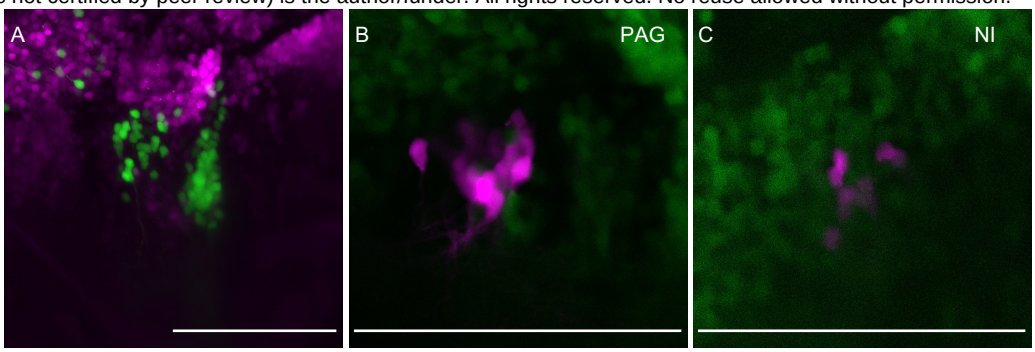

gsc2 neurons + glutamatergic neurons

glutamatergic neurons + *rln3a* neurons

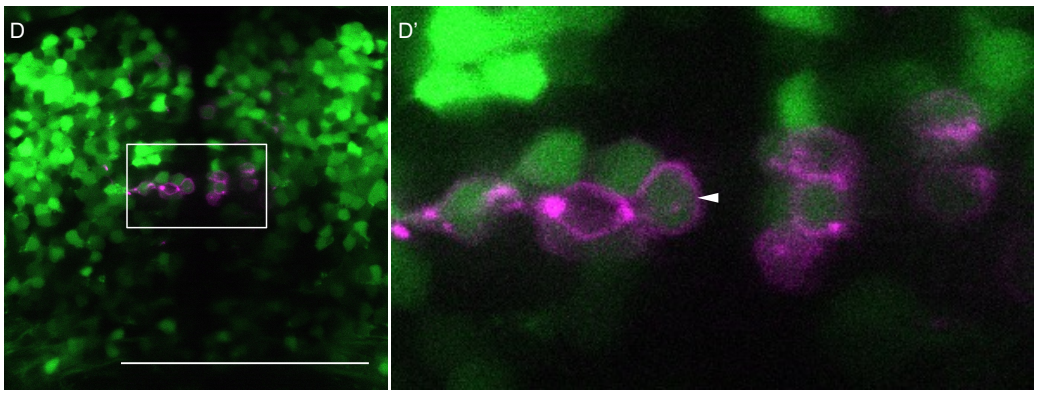

GABAerigc neurons + *gsc2* neurons

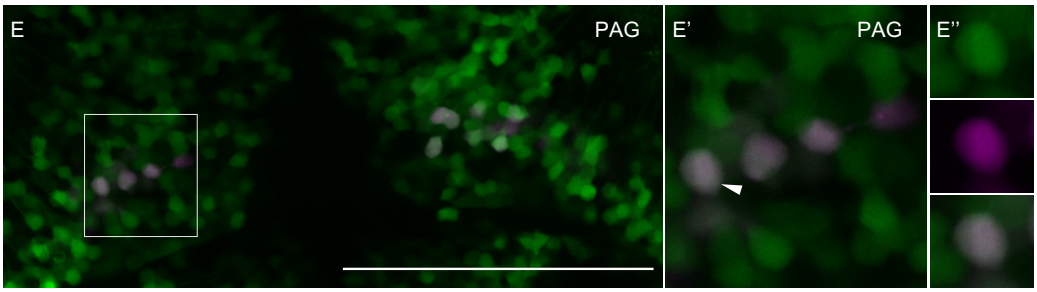

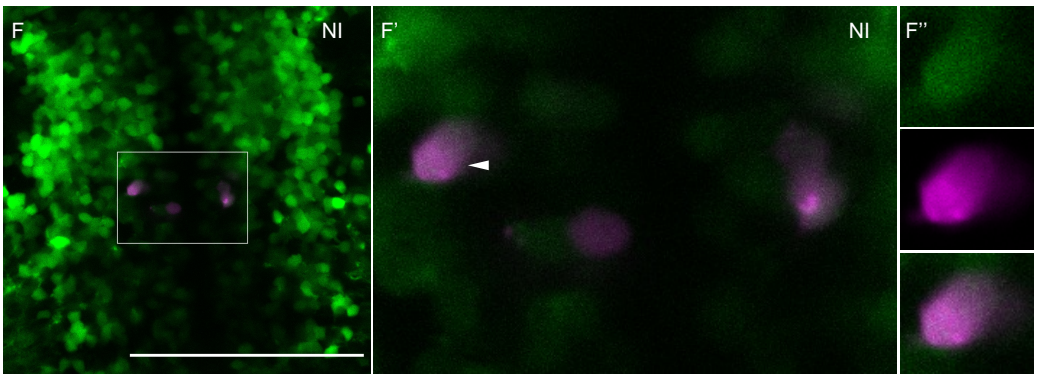

GABAerigc neurons + *rln3a* neurons

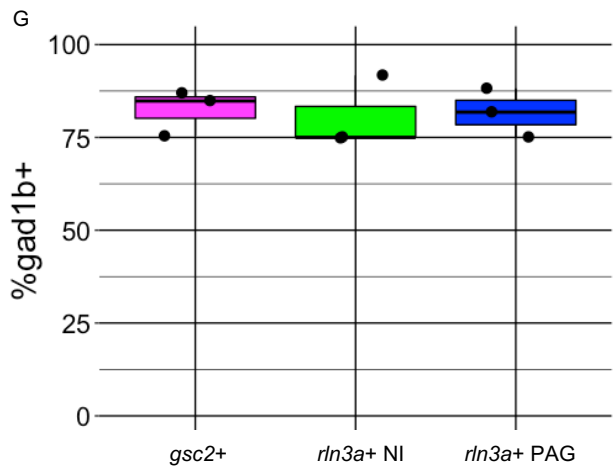

Figure 4

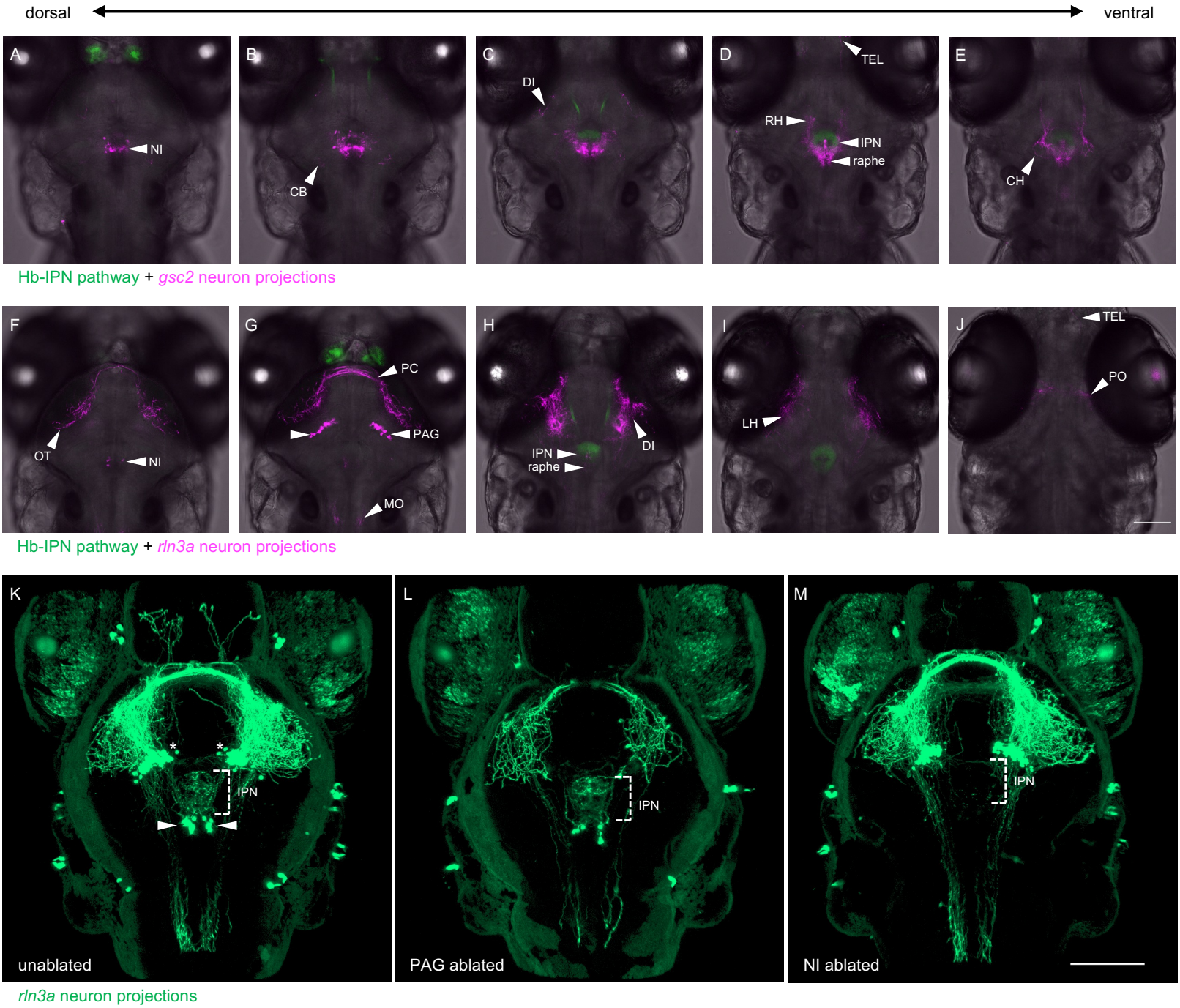
dorsal
ventral
A
NI
B
CB
C
DI
D
TEL
RH
IPN
raphe
E
CH
Hb-IPN pathway + gsc2 neuron projections
F
OT
NI
G
PC
PAG
MO
H
IPN
raphe
DI
I
LH
J
TEL
PO
Hb-IPN pathway + rln3a neuron projections
K
IPN
unablated
L
IPN
PAG ablated
M
IPN
NI ablated
rln3a neuron projections

Figure 5

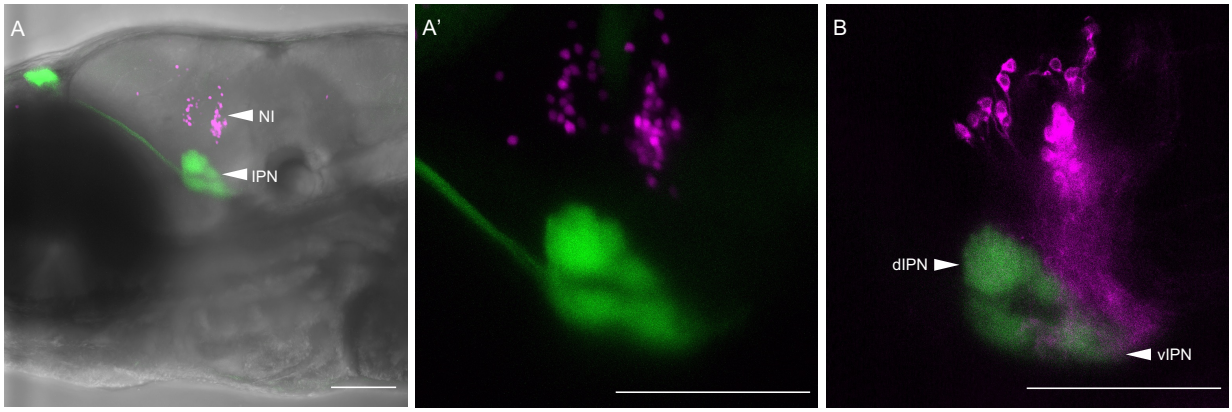

gsc2 neurons + Hb-IPN pathway

gsc2 neuron projections + IPN

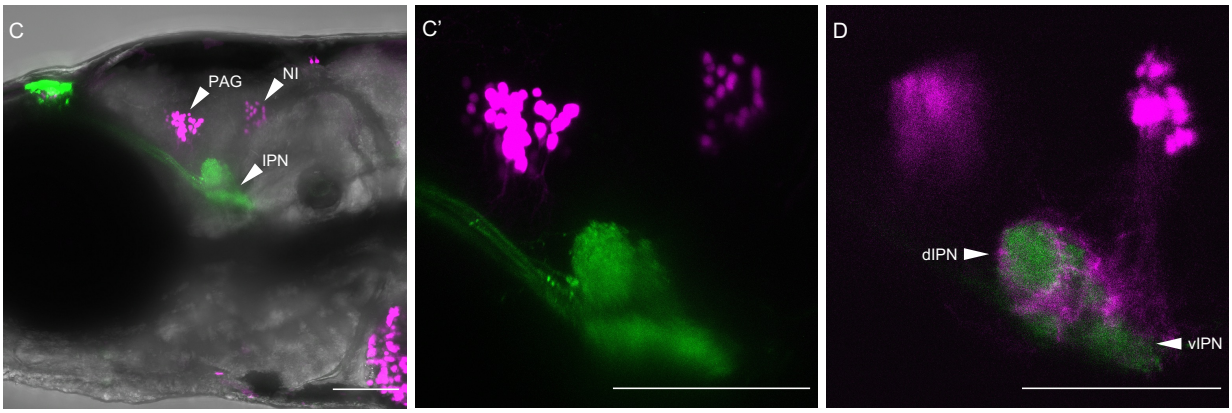

rln3a neurons + Hb-IPN pathway

rln3a neuron projections + IPN

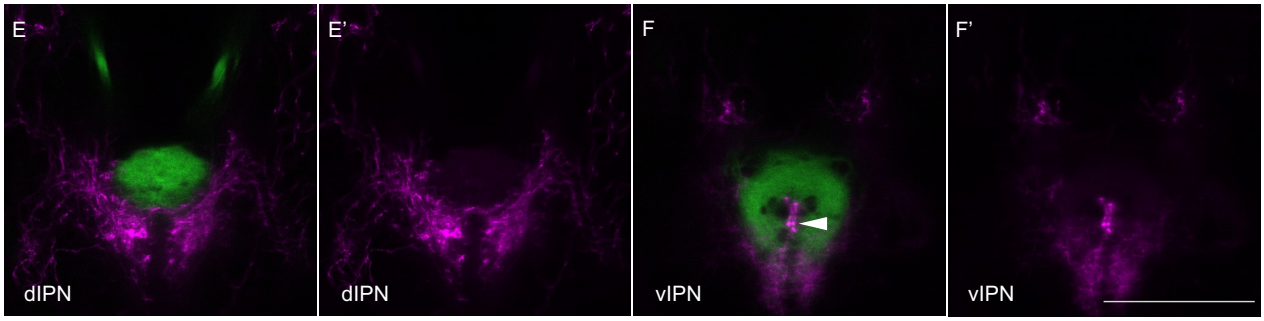

gsc2 neuron projections + IPN

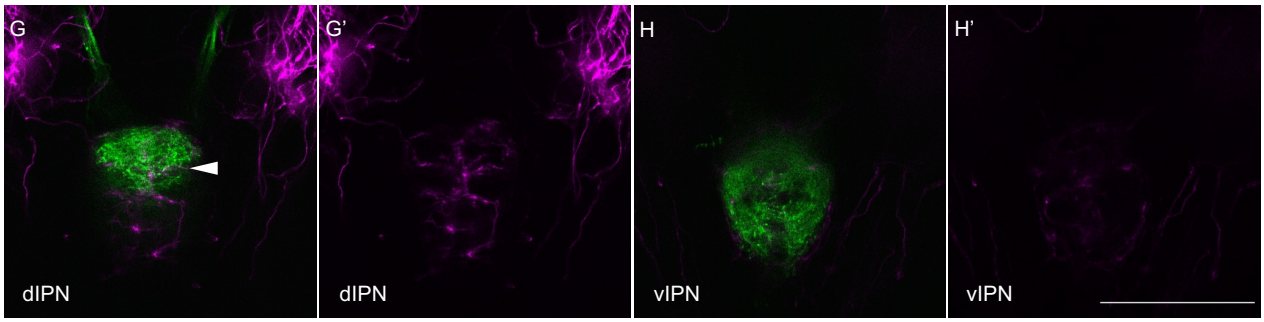

rln3a neuron projections + IPN

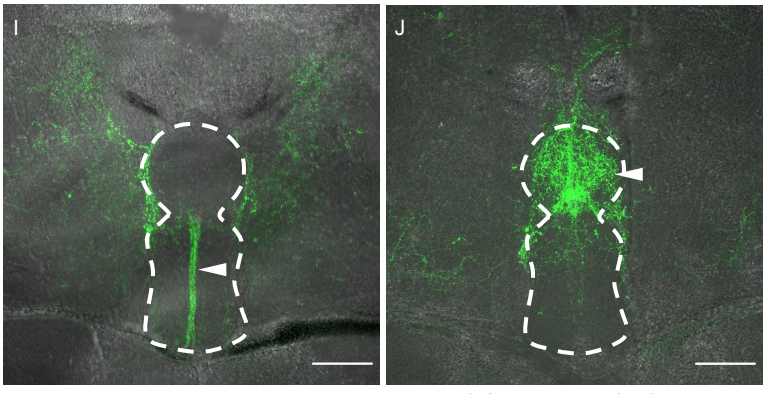

gsc2 neuron projections

rln3a neuron projections

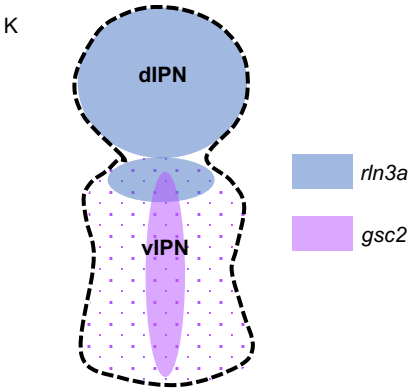

Figure 6

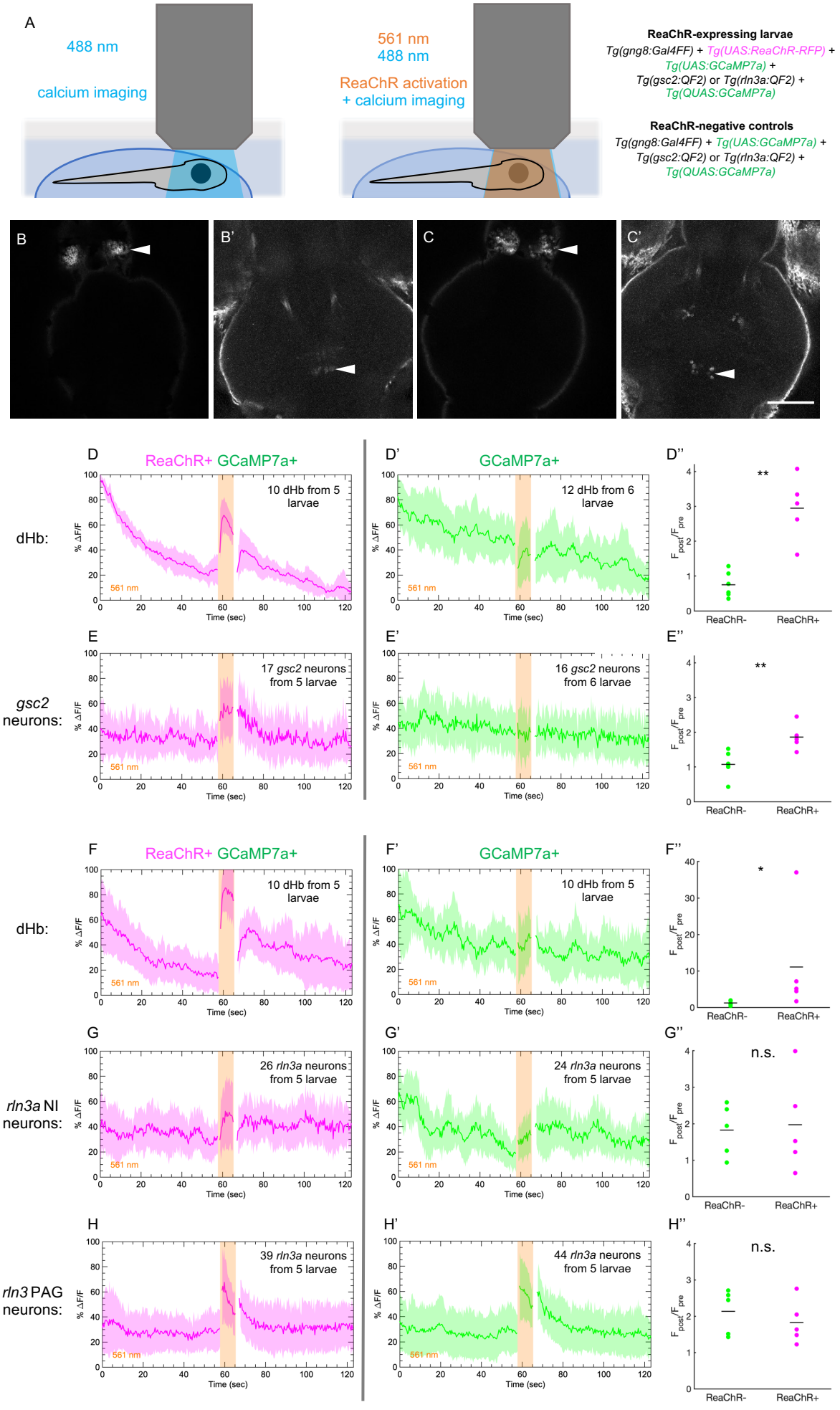
A
488 nm
calcium imaging
561 nm
488 nm
ReaChR activation
+ calcium imaging
ReaChR-expressing larvae
Tg(gng8:Gal4FF) + Tg(UAS:ReaChR-RFP) +
Tg(UAS:GCaMP7a) +
Tg(gsc2:QF2) or Tg(rln3a:QF2) +
Tg(QUAS:GCaMP7a)
ReaChR-negative controls
Tg(gng8:Gal4FF) + Tg(UAS:GCaMP7a) +
Tg(gsc2:QF2) or Tg(rln3a:QF2) +
Tg(QUAS:GCaMP7a)
B
B'
C
C'
D
ReaChR+ GCaMP7a+
10 dHb from 5 larvae
D'
GCaMP7a+
12 dHb from 6 larvae
D''
dHb:
E
17 gsc2 neurons from 5 larvae
E'
16 gsc2 neurons from 6 larvae
E''
gsc2 neurons:
F
10 dHb from 5 larvae
F'
10 dHb from 5 larvae
F''
dHb:
G
26 rln3a neurons from 5 larvae
G'
24 rln3a neurons from 5 larvae
G''
rln3a NI neurons:
H
39 rln3a neurons from 5 larvae
H'
44 rln3a neurons from 5 larvae
H''
rln3 PAG neurons:
% ΔF/F
Time (sec)
561 nm
ReaChR-
ReaChR+
n.s.

Figure 7

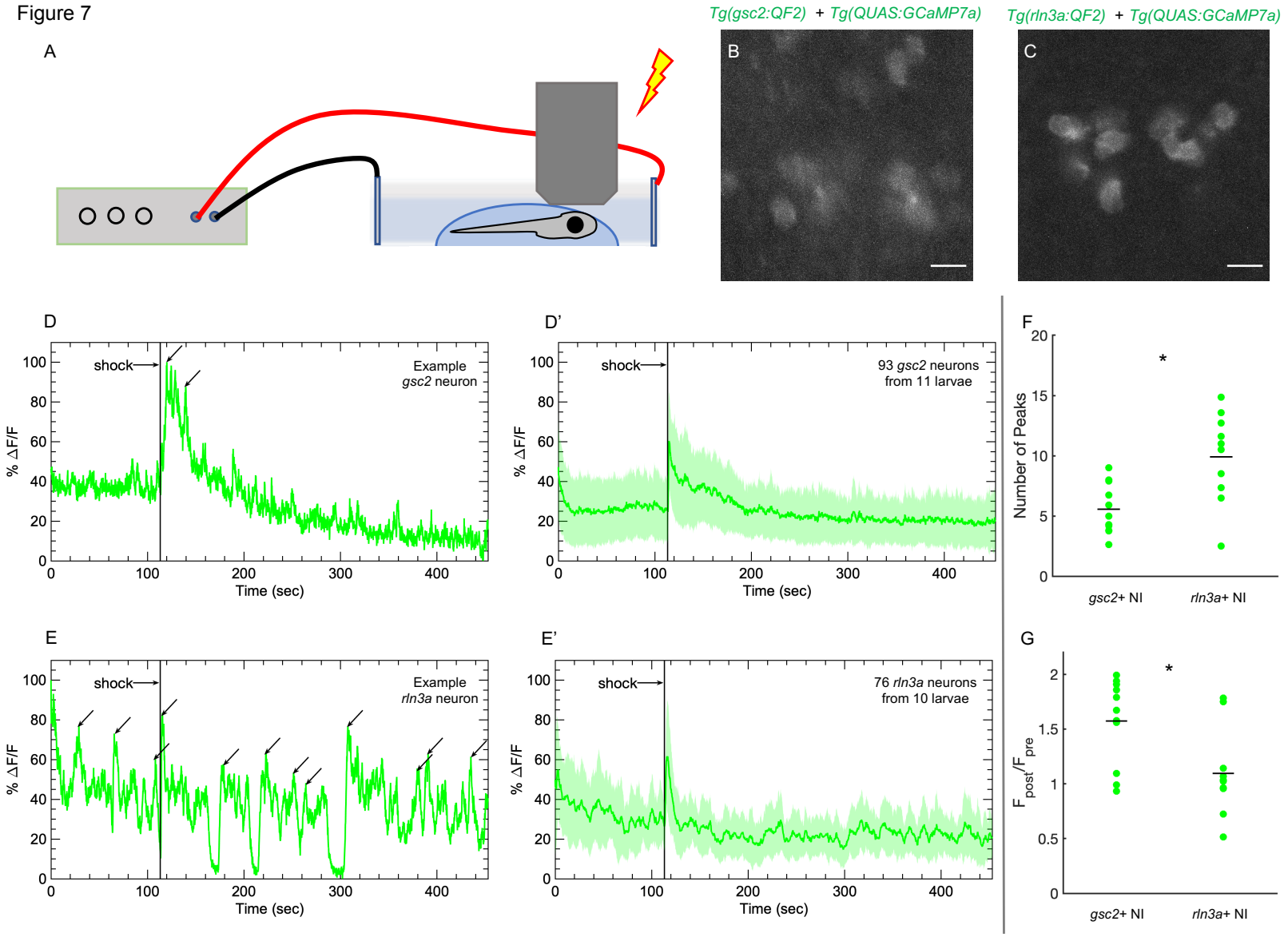
A
Tg(gsc2:QF2) + Tg(QUAS:GCaMP7a)
B
Tg(rln3a:QF2) + Tg(QUAS:GCaMP7a)
C
D
shock
Example gsc2 neuron
% ΔF/F
Time (sec)
D'
shock
93 gsc2 neurons from 11 larvae
% ΔF/F
Time (sec)
E
shock
Example rln3a neuron
% ΔF/F
Time (sec)
E'
shock
76 rln3a neurons from 10 larvae
% ΔF/F
Time (sec)
F
Number of Peaks
*
gsc2+ NI
rln3a+ NI
G
F post/F pre
*
gsc2+ NI
rln3a+ NI

Figure 8

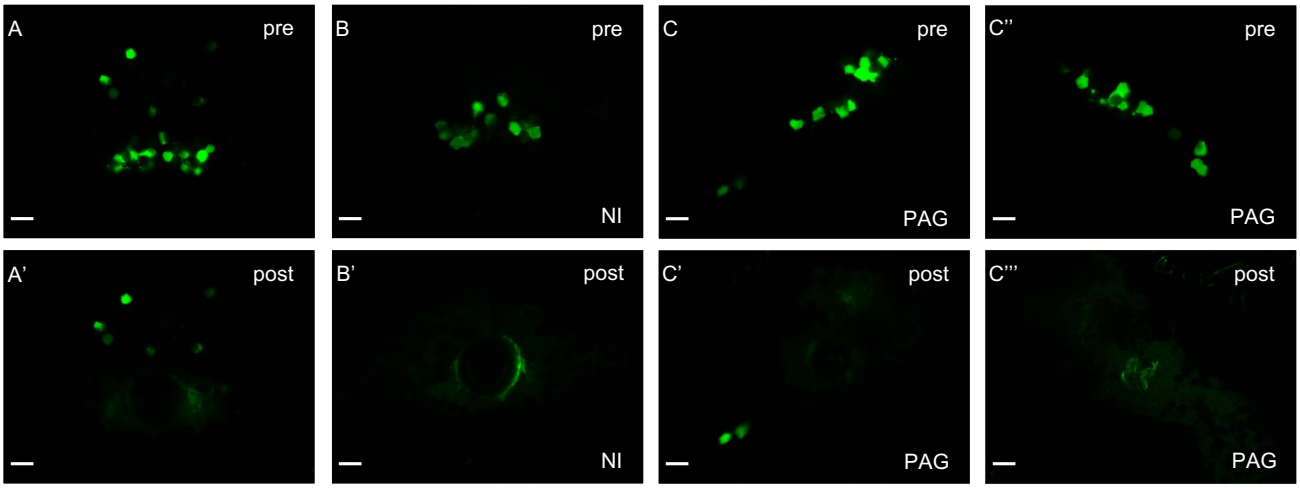

Tg(gsc2:QF2) + *Tg(QUAS:GFP)* *Tg(rln3a:QF2)* + *Tg(QUAS:GFP)*

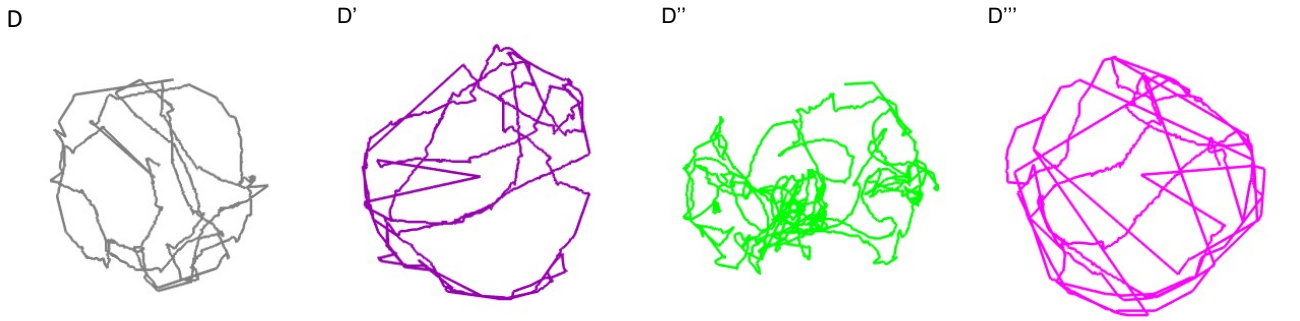

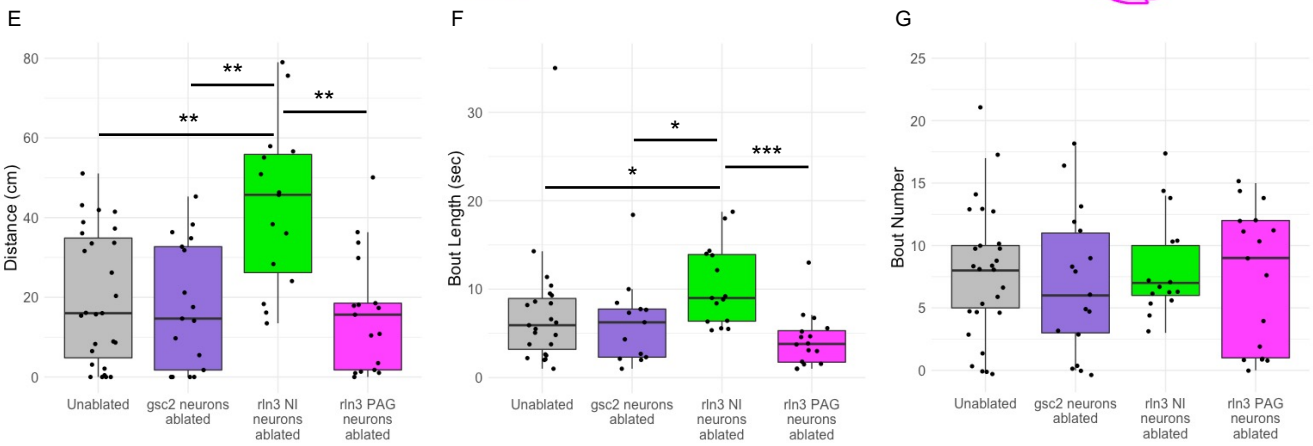

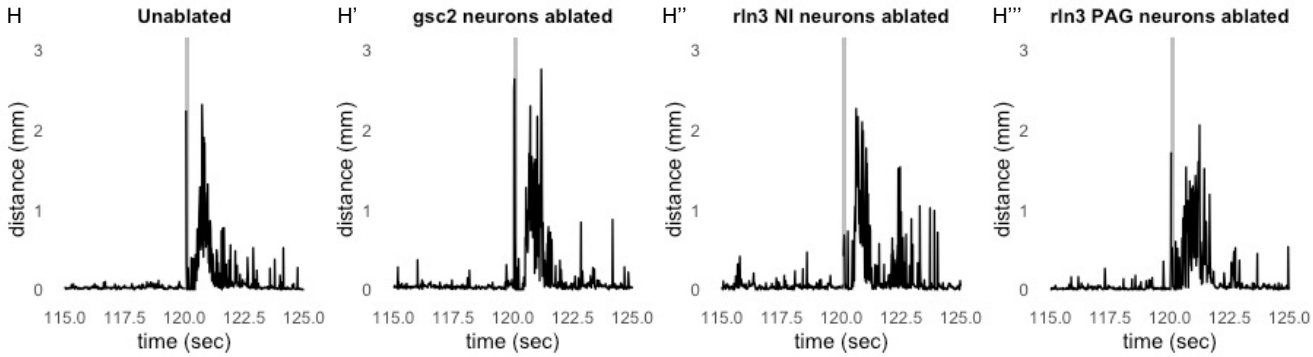

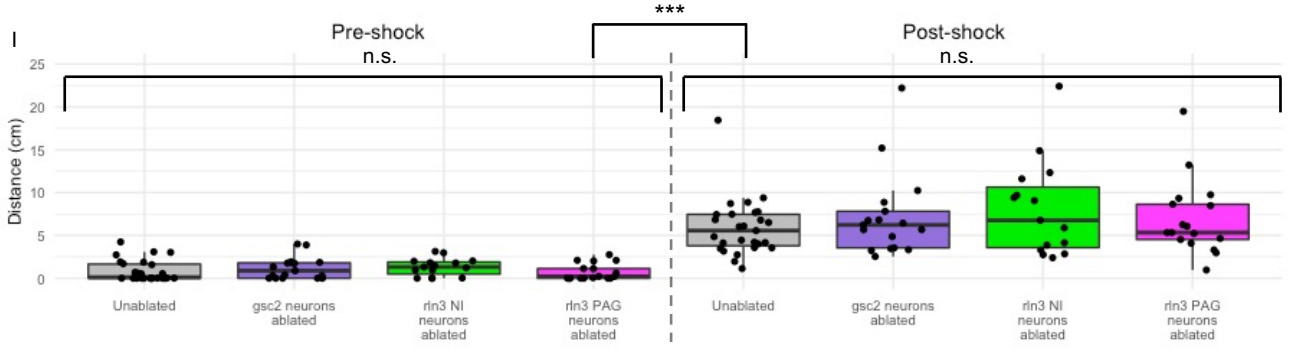

Supplementary Figure 1

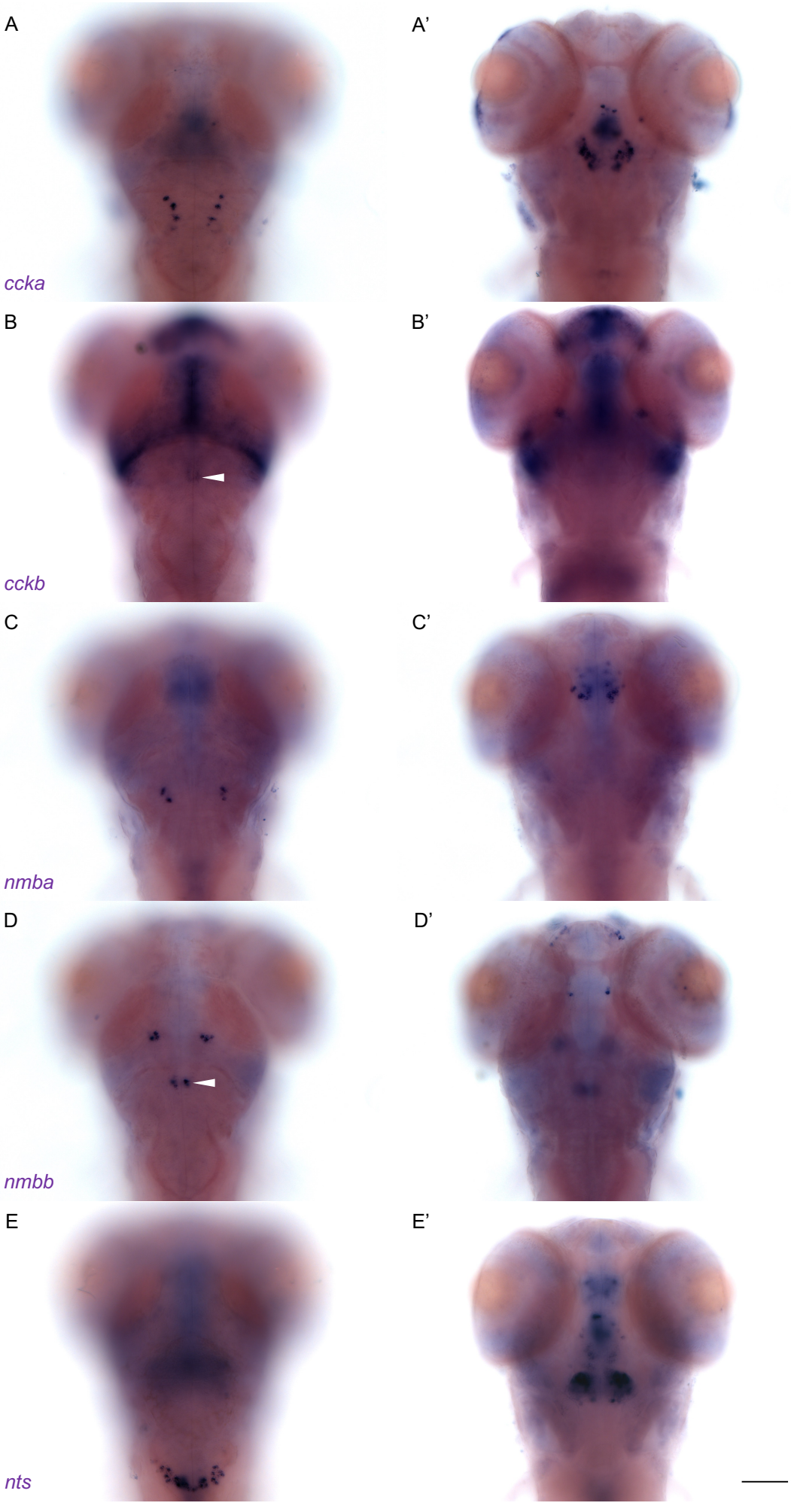

Supplementary Figure 2

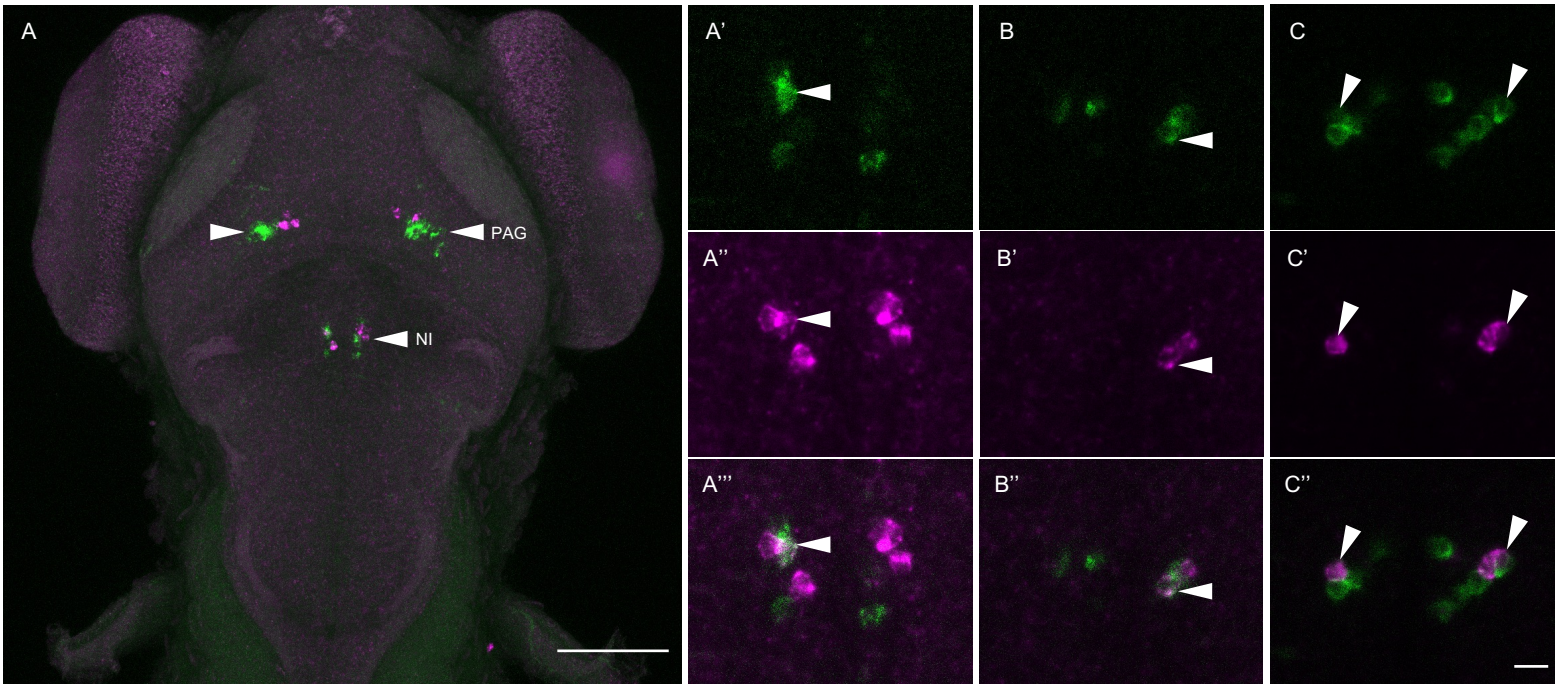

rln3a + *nmbb*

Supplementary Figure 3

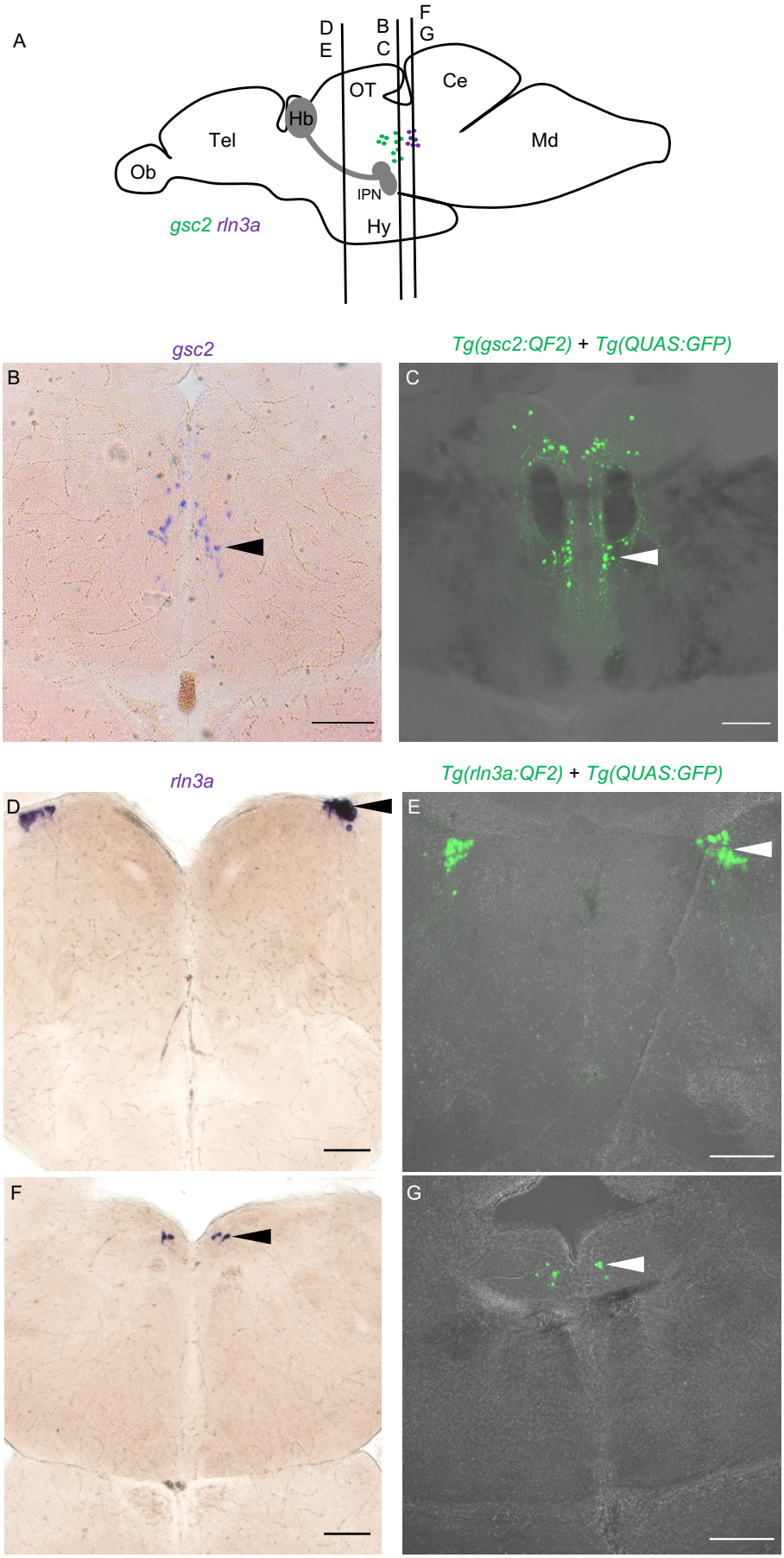

Supplementary Figure 4

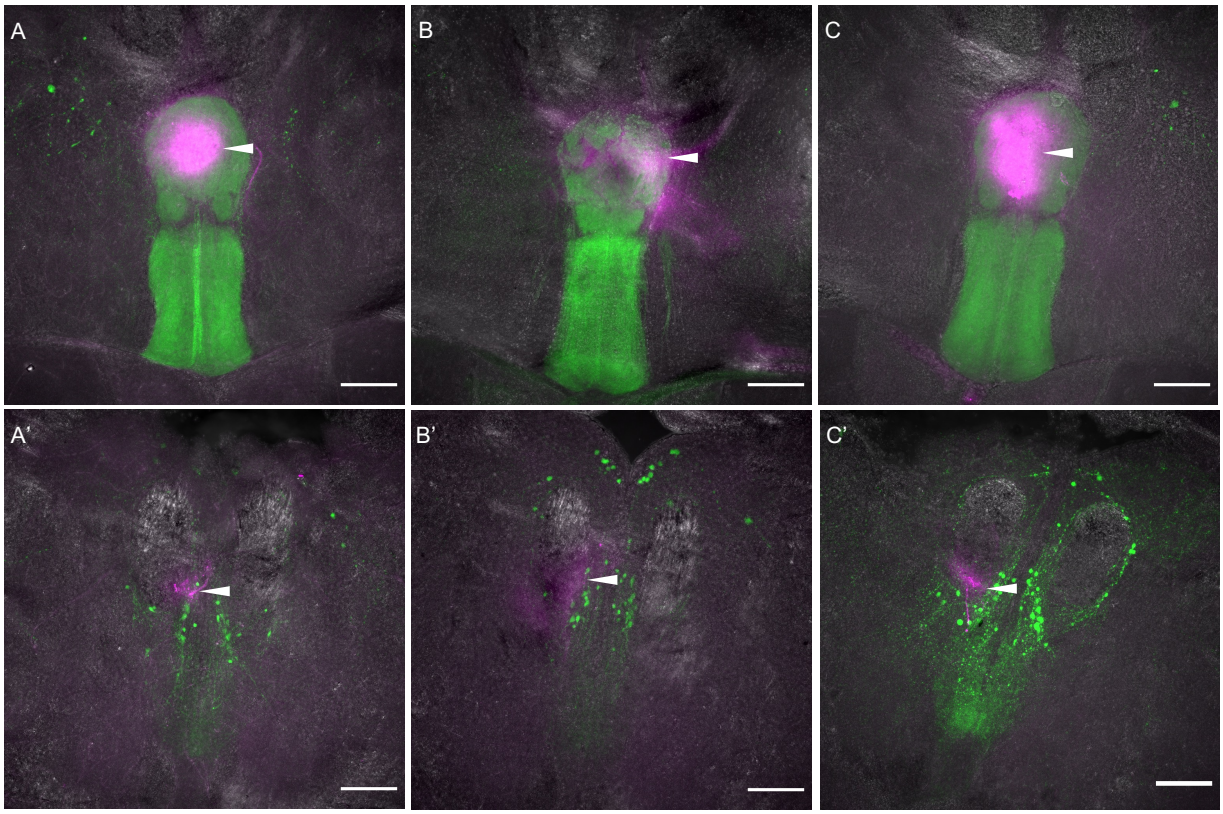

Tg(gng8:GFP-CAAX) + *Tg(gsc2:QF2)* + *Tg(QUAS:GFP)* + DiI

Supplementary Figure 5